Received: 29 July 2021 | Revised: 26 July 2023 | Accepted: 27 July 2023

DOI: 10.1111/bre.12814

Basin Research | IAS EAGE | WILEY

RESEARCH ARTICLE

Joint application of fluid inclusion and clumped isotope (Δ_{47}) thermometry unravels the complexity of thermal and fluid-flow history reconstruction in sedimentary basins—Upper Triassic Chaunoy Formation reservoirs (Paris Basin)

Natalia A. Vergara Sassarini[1,2,3] | **Marta Gasparrini**[4] | **Stefano M. Bernasconi**[5] | **Sveva Corrado**[1]

[1]Department of Sciences, University of Roma Tre, Rome, Italy

[2]IFP Energies nouvelles, Rueil-Malmaison, France

[3]Sorbonne Université, Paris, France

[4]Earth Sciences Department, University of Milan, Milan, Italy

[5]Geological Institute, ETH Zurich, Zürich, Switzerland

Correspondence
Marta Gasparrini, Earth Sciences Department, University of Milan, Via Mangiagalli 34, Milan 20133, Italy.
Email: marta.gasparrini@unimi.it

Present address
Natalia A. Vergara Sassarini, Center of Studies and Activities for Space (CISAS) "G. Colombo", University of Padua, Padua, Italy

Funding information
IFP Energies nouvelles; Ministero dell'Istruzione, dell'Università e della Ricerca (MIUR)

Abstract

We investigated calcites and dolomites precipitated during burial diagenesis of the Upper Triassic (Norian) continental siliciclastics from sub-surface reservoirs of the northern Paris Basin (Chaunoy Formation) that experienced a thermal maximum >100°C during Late Cretaceous times. Relative carbonate precipitation timing was established via petrographic analyses. The diagenetic carbonates were further investigated by fluid inclusion and clumped isotope (Δ_{47}) thermometry. The two thermometric datasets were interpreted by evaluating the possible occurrence of inclusion thermal reequilibration and Δ_{47} solid-state reordering, based on the known basin thermal history and the three existing Δ_{47} reordering models. By considering the fluid inclusion and Δ_{47} datasets obtained and the various Δ_{47} reordering models, different carbonate precipitation scenarios, in terms of timing and parent fluid composition ($\delta^{18}O_{fluid}$), were inferred. These results underline that in samples having experienced thermal maximum >100°C, accuracy and interpretation of fluid inclusion and Δ_{47} thermometry data (especially on calcite) may be biased by thermal reequilibration and solid-state reordering. The results converge towards the need of jointly applying fluid inclusion and Δ_{47} thermometry on the same carbonate phases to evaluate all the possible precipitation scenarios. The most likely carbonate precipitation scenarios, based on Δ_{47} thermometry data, point at the precipitation of two calcite phases during Early to Late Jurassic times and of one dolomite phase during the Late Cretaceous. The parent fluids possibly were original formation waters of the Chaunoy Fm. that mixed with brines migrating from the East, where time equivalent evaporitic deposits occur. The proposed precipitation model for calcites and dolomites, involving different pulses of brine migration, and the dominance of calcite phases were not recorded by previous studies on the Upper Triassic units. These latter results

may be of interest to evaluate the reservoir potential of the Chaunoy Fm. in this underexplored portion of the Paris Basin.

KEYWORDS

burial diagenetic carbonates, Chaunoy Formation, fluid inclusion reequilibration, Paris Basin, sedimentary basin thermal history, Δ_{47} reordering

1 | INTRODUCTION

Diagenetic carbonates are fossil witnesses of past hydrogeology in sedimentary basins and their study may unravel the conditions (temperature, $\delta^{18}O_{fluid}$, salinity) of the parent fluids which have induced their precipitation (e.g., Allan & Wiggings, 1993; Morse & Mckenzie, 1990). Reconstructing the precipitation conditions of diagenetic carbonates plays a crucial role in the assessment of trustworthy conceptual models aiming to predict their occurrence in space and time and consequently the heterogeneities in petrophysical properties of both carbonate and siliciclastic reservoir rocks (Moore, 2001; Worden et al., 2018). Therefore, reconstructing the origin of past fluid flows responsible for the precipitation of carbonate diagenetic phases is key to predict their distribution at basin scale from an exploration perspective of both fossil and renewable resources (Deschamps et al., 2012; Morad, 1998).

The precipitation conditions of diagenetic carbonates, and specifically the temperature, were historically inferred by using: (1) oxygen isotope exchanges between carbonates and fluids at equilibrium (O'Neil et al., 1969; Sharp & Kirschner, 1994); (2) fluid inclusion microthermometry (FIM; Roedder & Bodnar, 1980; Goldstein & Reynolds, 1994). However, these tools are subject to several application limits, potentially affecting the reliability of the reconstructed conceptual models. The confident use of the first thermometer requires independent knowledge of the oxygen isotope composition of the fluids ($\delta^{18}O_{fluid}$) that may significantly vary in time and space, especially for burial diagenetic fluids (e.g., Hanor, 1984; Kharaka & Hanor, 2003). Conversely, the confident use of the FI thermometer may be limited by several factors including crystal optical properties (e.g., turbidity, coarseness, and birifrangence), FI petrography (e.g., occurrence, size, shape) and metastability, as well as post-entrapment processes such as necking down, stretching or leakage due to thermal reequilibration among others (Bodnar, 2003; Goldstein, 2001, 2003; Goldstein & Reynolds, 1994).

More recently, the development of the carbonate clumped isotope technique (Eiler, 2007; Ghosh et al., 2006; Schauble et al., 2006), referred to as Δ_{47}, opened the way to independently unravel both precipitation temperature ($T(\Delta_{47})$) and parent fluid composition ($\delta^{18}O_{fluid}$). However, original Δ_{47} compositions acquired at the time of carbonate precipitation may be susceptible to resetting due to the Δ_{47} solid-state reordering process. This process occurs in samples exposed to significant heating for an extended period and primarily depends on the temperature–time path followed by the samples and on the mineralogy of the carbonate phase considered (e.g. Brenner et al., 2018; Hemingway & Henkes, 2021; Huntington & Petersen, 2023; Lawson et al., 2018; Lloyd et al., 2018; Mangenot et al., 2019; Passey & Henkes, 2012; Stolper & Eiler, 2015).

Both FI and Δ_{47} thermometry techniques have, therefore, limitations that need to be considered, as they impact the characterization of paleo-fluids, and, consequently the realistic reconstruction of the thermal and fluid-flow history of sedimentary basins. FI and Δ_{47} analyses may be accomplished on the same burial diagenetic carbonates to evaluate the mutual consistency of the thermal data obtained from the two techniques (Honlet et al., 2018; Jautzy et al., 2021; MacDonald et al., 2018; Mangenot et al., 2017). This may contribute to a better understanding of the FI and Δ_{47} behaviour during the thermal evolution of sedimentary basins. In particular, joint application of FI and Δ_{47} analysis on burial diagenetic carbonates from the Middle Jurassic reservoirs of the Paris Basin depocenter, that experienced a thermal maximum of ca. 90°C, revealed mutual consistency suggesting that neither thermal reequilibration of FI nor solid-state reordering of Δ_{47} had occurred. These data led to an accurate determination

Highlights

- Δ_{47} and fluid inclusion thermometry applied on samples being heated at T > 100°C.
- Evaluation of Δ_{47} solid-state reordering and inclusion thermal reequilibration.
- Calcite thermometry data may be biased by fluid inclusion thermal reequilibration and Δ_{47} solid-state reordering.
- Brine migration from the East caused calcite/dolomite precipitation in Jurassic/Cretaceous times.

of temperature, $\delta^{18}O_{fluid}$ and salinity of the parent fluids (Dassié et al., 2018; Mangenot et al., 2017) and paved the ground to unravel new information on thermal and fluid-flow histories of these reservoirs (Mangenot, Gasparrini, Gerdes, et al., 2018; Mangenot, Gasparrini, Rouchon, & Bonifacie, 2018). The Paris Basin represents thus an ideal target to further explore the applicability and limitations of FI and Δ_{47} thermometry in rock successions that underwent a more severe thermal history, characterized by a higher thermal maximum.

In the present survey, stratigraphically lower reservoirs (Upper Triassic Chaunoy Fm.), located to the NW of the Paris Basin depocenter, were investigated since, based on the most updated basin thermal model (Torelli et al., 2020), these rocks experienced a thermal maximum >100°C. The main aims were to jointly apply FI and Δ_{47} thermometry on burial diagenetic carbonates within these stratigraphically lower (and hotter) reservoirs to test the consistency of the data from the two techniques and evaluate the carbonate precipitation scenarios derived from the different datasets. As a by-product, this survey furnishes novel information on the diagenetic history of the Chaunoy Fm. reservoirs in an underexplored portion of the basin.

2 | GEOLOGICAL FRAMEWORK

2.1 | General geological setting

The Paris Basin, situated in northern France, is an intracontinental sedimentary basin with an approximate area of 110,000 km^2. The basin is bounded by the Armorican Massif in the W, the Ardennes Massif in the NE, and the Vosges Mountains in the E where the Hercynian basement crops out (Figure 1). The basin depocenter is filled by up to 3000 m of Permian to Quaternary deposits laying on the deformed Permian basement, which represents the northern branch of the Hercynian belt (Brunet & Le Pichon, 1982; Guillocheau et al., 2000; Perrodon & Zabek, 1991; Pomerol, 1989; Figure 1).

Rifting started to the E during Permian times with a general collapse of the Hercynian belt (André et al., 2010; Guillocheau et al., 2000; Perrodon & Zabek, 1991). During Triassic times, a period of renewed crustal stretching led to the fragmentation of the post-Hercynian peneplain, which separated the major stable Armorican, Vosgues, and Ardennes blocks. The Late Triassic (Carnian) was marked by a westward displacement of the subsidence centre towards the present-day basin depocenter (Guillocheau et al., 2000; Perrodon & Zabek, 1991). From Early to Middle Jurassic times the basin experienced a relatively rapid subsidence rate (20–25 m/My; Perrodon & Zabek, 1991) related to the Early- to Mid-Cimmerian events marking the beginning of the Ligurian Tethys rifting (Early Cimmerian) and ocean accretion (Middle Cimmerian; André et al., 2010; Perrodon & Zabek, 1991). Contemporaneous to the Tethys accretion, the Aalenian unconformity (also referred to as Middle Cimmerian unconformity; Ziegler, 1990) registered the early stage rising of the thermal dome in the central North Sea (André et al., 2010; Guillocheau et al., 2000). During Late Jurassic times (Kimmeridgian to Tithonian), a decrease in subsidence rate was promoted by a shift towards a high wavelength flexural pattern, possibly associated with the opening of the Central Atlantic Ocean (Guillocheau et al., 2000). The subsidence decreased gradually until the Early Cretaceous (Berriasian to Late Aptian) when a significant decrease in the subsidence rate occurred (0–10 m/My; Guillocheau et al., 2000; Perrodon & Zabek, 1991). The Late Jurassic-Early Cretaceous transition was bounded by two major Jurassic/Cretaceous (Late Cimmerian) and Early/Late Berriasian (Austrian) unconformities (André et al., 2010; Guillocheau et al., 2000; Perrodon & Zabek, 1991). These unconformities, caused by NE-SW to E-W compression, formed contemporaneously with both the uplift of the Vosgues-Rhine block to the NE and with the extension (Late Cimmerian) and further oceanic accretion (Austrian) in the Bay of Biscay (Guillocheau et al., 2000). After an extensional period of subsidence from Albian to Turonian, NE-SW compression began in Late Turonian. At the Cretaceous-Paleogene boundary, the main tectonic inversion occurred resulting in significant uplift and erosion. The last main tectonic event took place during the Late Eocene to Early Oligocene and was marked by E-W extension in the eastern part of the basin (Rhine Graben opening), while a compressive regime prevailed in the western part (André et al., 2010; Guillocheau et al., 2000).

The Triassic stratigraphy was mainly dominated by a transgressive trend. The Lower Triassic developed to the East and was characterized by coarse red sandstones associated with fluvial channel deposition (Perrodon & Zabek, 1991). During the Middle Triassic, sedimentation migrated towards the central part of the basin where a very shallow epicontinental sea transgressed from the E, with the deposition of marine sandstones overlaid by marine limestones and dolomites, and locally by anhydrite-bearing shales (Perrodon & Zabek, 1991). In the Upper Triassic, sedimentation began with the deposition of the Carnian fluvial sandstones (Figure 1c; Bourquin et al., 1998; Perrodon & Zabek, 1991). During the Norian, towards the western portion of the basin, the sedimentation of the braided alluvial fans to lacustrine deposits of the Chaunoy Fm. occurred. These deposits, formed in semi-arid to arid conditions (Bourquin et al., 1998; Spötl & Wright, 1992; Worden et al., 1999), exhibit a range of lithologies, comprising fine to coarse continental terrigenous

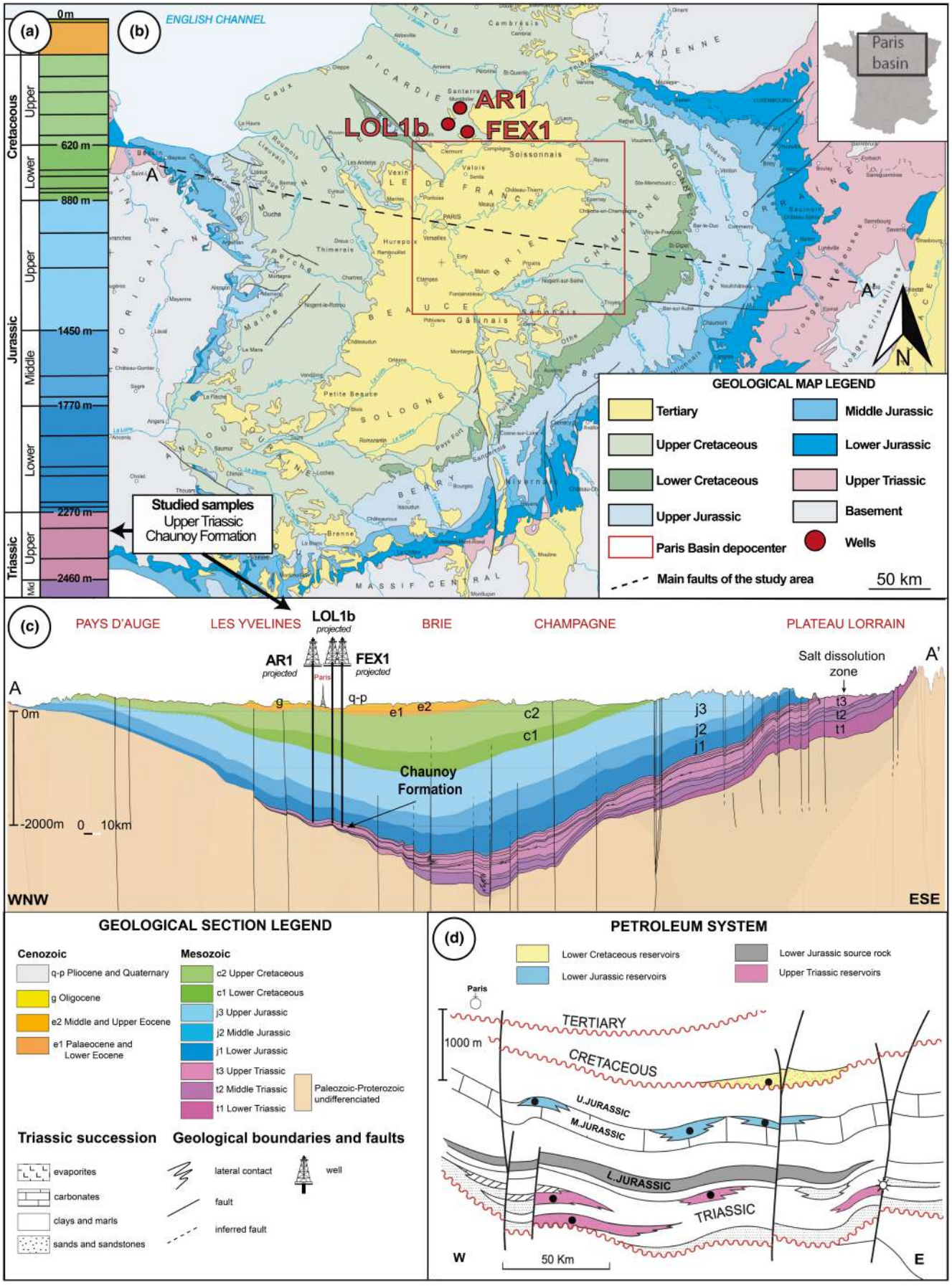

FIGURE 1 Geographic and geological setting of the study area in the Paris Basin. (a) Stratigraphic column of the Paris Basin sedimentary pile (from FEX1 well). (b) Location of the Paris Basin in northern France (upper right frame). Geological map of the Paris Basin (modified after Gély & Hanot, 2014) with location of the basin depocenter and the three studied wells (LOL1b, AR1, FEX1). The dashed black line represents the trace of the cross-section illustrated in c. (c) WNW-ESE geological cross-section of the Paris Basin illustrating the three projected wells of interest and the stratigraphic interval corresponding to the Upper Triassic (Norian) Chaunoy Fm. (modified after Delmas et al., 2002). (d) Schematic W-E cross-section of the Paris Basin petroleum system, illustrating the main source rocks and reservoirs (modified after Delmas et al., 2002).

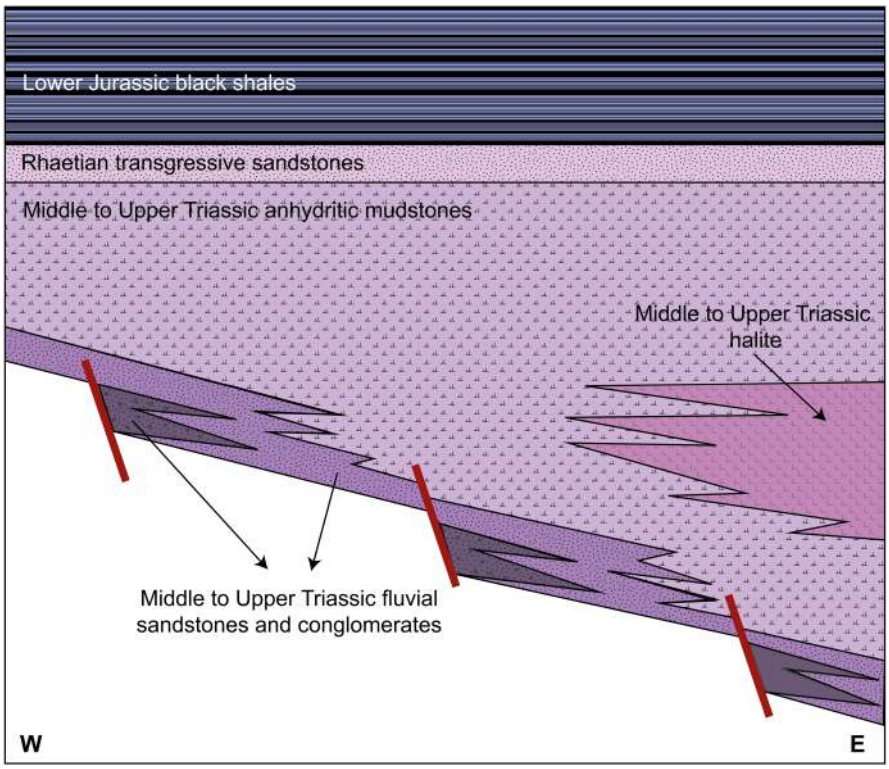

FIGURE 2 Simplified geologic sketch illustrating the lateral facies changes of the Middle Triassic to Lower Jurassic succession along a W-E transect through the Paris Basin. The Chaunoy Formation occurs to the West and is comprised among the fluvial sandstones and conglomerates; to the East it passes laterally to anhydritic mudstones and halite deposits (redrawn after Worden et al., 1999).

facies (clays, fine to coarse fluvial sandstones, conglomerates) with some interbedded carbonate mudstones and dolomites (Bourquin et al., 1993, 1997, 1998). The Chaunoy Fm. is extensively cemented by early carbonates and locally includes pedogenic dolocrete horizons (Bourquin et al., 1998; Spötl & Wright, 1992). Towards the eastern portion of the basin, the Chaunoy deposits pass laterally into a time equivalent marine halite succession which interfingers with the western fluvial sandstones separated by interbedded coastal sabkha sands and anhydritic mudstones (Figure 2; Bourquin et al., 1998; Cavelier & Lorenz, 1987; Geisler-Cussey, 1986).

The Triassic sedimentation ended with the deposition of the Rhaetian transgressive sandstones, deposited in deltaic and nearshore environments (Keuper strata; Perrodon & Zabek, 1991). By the end of the Triassic, the basin was an N-E trending sag depression with an average sediment thickness of ca. 500 m. During Early Jurassic times, organic-rich black shales were deposited due to a widespread transgression. In the Middle Jurassic, broad carbonate platforms prevailed, while the Upper Jurassic was primarily characterized by clay deposition (Guillocheau et al., 2000; Perrodon & Zabek, 1991). During the Late Cretaceous (Berriasian to Albian), mainly siliciclastic deposits with well-developed deltaic and coastal plain facies dominated. The Albian-Cenomanian transition was characterized by a transgressive-regressive cycle which accounted for siliciclastic tidal-dominated facies followed by chalk. After the sedimentation of the thick Upper Cretaceous chalk, the eastern part of the Paris Basin definitively emerged and experienced weathering and erosion allowing the progressive exhumation of the underlying units (Guillocheau et al., 2000; Perrodon & Zabek, 1991).

In the central part of the Paris Basin two main permeable reservoir units occur: the Upper Triassic (Norian) fluvial sandstones of the Chaunoy Fm., and the Middle Jurassic marine carbonates (Figure 1d; (Delmas et al., 2002; Pages, 1987). Between the Upper Triassic silicisclastics and the Middle Jurassic carbonates are the Lower Jurassic (Toarcian) shales (Figure 1d) which represent the main source rocks of the basin having charged with hydrocarbons both the Upper Triassic and the Middle Jurassic reservoirs (Delmas et al., 2002; Poulet & Espitalié, 1987). More recently, these reservoirs have received the attention of the

European geothermal community (Ledésert et al., 2022) with the Chaunoy Fm. at an early exploration stage (Boissavy & Grière, 2014; Bonté et al., 2013; Jaudin, 2009; Sengelen et al., 2019, 2021).

2.2 | Thermal history and models

The thermal evolution of the Paris Basin has been robustly characterized on natural rock samples by means of various thermometric and thermo-chronometric proxies, including among others Rock-Eval pyrolysis, vitrinite reflectance, fluid inclusion microthermometry, apatite fission tracks, clay diagenesis, Δ_{47} thermometry and U-Pb carbonate geochronology (Blaise et al., 2014; Clauer et al., 1995; Espitalié et al., 1988; Guilhaumou, 1993; Guilhaumou & Gaulier, 1991; Mangenot, Gasparrini, Gerdes, et al., 2018; Mangenot, Gasparrini, Rouchon, & Bonifacie, 2018; Matray et al., 1989; Ménétrier et al., 2005; Poulet & Espitalié, 1987; Spötl, 1996; Spötl et al., 1993; Uriarte, 1997). These proxies were used to build, validate and calibrate numerical 1D, 2D and 3D basin thermal models (Gaulier & Burrus, 1994; Gonçalvès et al., 2010; Monticone et al., 2011; Telès et al., 2014; Torelli et al., 2020; Uriarte, 1997; Worden et al., 1999). All these previous data and numerical models make the burial and thermal history of the basin well-constrained.

The most recent 3D numerical model of the Paris Basin, furnished by Torelli et al. (2020), was developed using the TemisFlow™ software and was built upon the geological model previously constructed by Telès et al. (2014). The reliability of the model from Torelli et al. (2020) is ensured by the fact that it considers multiple parameters, including surface temperature and paleo-bathymetry evolution, a detailed reconstruction of sediment deposition and erosion events, basal heat flow, and thermal properties of the rocks filling the basin. In order to consider the impact of compositional heterogeneities of the basement lithology on the basin thermal state, the model also incorporates an upper crust comprising three domains characterized by different thicknesses, radiogenic heat production and conductivity.

The thermal properties at the output of the model (i.e., present-day and past temperatures) were calibrated to find the best fit with thermometric data available from literature. These latter encompassed the present-day bottom hole temperatures from 52 wells (Gable, 1978) and the vitrinite reflectance data from Uriarte (1997), which are consistent with recently obtained vitrinite reflectance data (Corrado et al., 2022; Vergara Sassarini, 2022; Vergara Sassarini et al., 2023). Furthermore, the burial histories extracted from the model were found to be consistent with independent constraints derived from stylolite paleo-piezometry (Beaudoin et al., 2019). We, therefore, relied on the thermal model from Torelli et al. (2020) to interpret and discuss the thermal data issued from the present study.

According to this model, the basin succession underwent progressive burial and heating during the Mesozoic, followed by uplift and cooling that started in the Late Cretaceous and continued during the whole Tertiary. The thermal maximum occurred during the Late Cretaceous and persisted for approximately 20 million years. The thermal conditions recorded in the basin during the Late Cretaceous are most commonly attributed to the deposition of a thick chalk succession (see Section 2.1) with very low thermal conductivity, which acted as a thermal insulator causing an increase of the geothermal gradient in the underlying deposits (Demars & Pagel, 1994; Guilhaumou, 1993; Ménétrier et al., 2005; Spötl et al., 1993; Torelli et al., 2020).

3 | MATERIALS AND METHODS

3.1 | Sampling

The study area was selected based on the availability of sub-surface cores from the depocentral area of the Paris Basin where the Upper Triassic succession is known to have experienced a thermal maximum >100°C (Torelli et al., 2020) that was a needed prerequisite for our aims (see Section 1). Being the Chaunoy Fm. a past target for oil and gas exploration, most of the available cores were from this stratigraphic interval that was therefore chosen for observation and sampling. Only three discontinuous cores of the Chaunoy Fm., from barren wells located to the NW of the basin depocenter (Figure 1b,c), revealed the occurrence of diagenetic carbonates macroscopically visible. This guided the sampling strategy since for our aims (see Section 1) voluminous carbonate phases were needed to jointly investigate them by petrography, O-C isotope geochemistry as well as by FI and Δ_{47} thermometry. Based on stratigraphic correlations available from the well logs drilling reports of these three wells (Longueil1b (LOL1b), Arsy1 (AR1), and Feigneux1 (FEX1); Figure 3) the Chaunoy Fm. was identified and sampled. A total of 16 samples, encompassing different facies of the Chaunoy Fm., were collected (Figure 3; Table 1). Sample depths vary between 2002 and 2009 m at LOL1b ($n = 6$), between 1819 and 1826 m at AR1 ($n = 4$), and between 2370 and 2408 m at FEX1 ($n = 6$). The samples belong to different facies ascribed to different depositional environments, based on Bourquin et al. (1998). The main facies include channel-infilling clast-supported conglomerates (Figure 4a) and fine to very coarse-grained sandstones (Figure 4b), as well

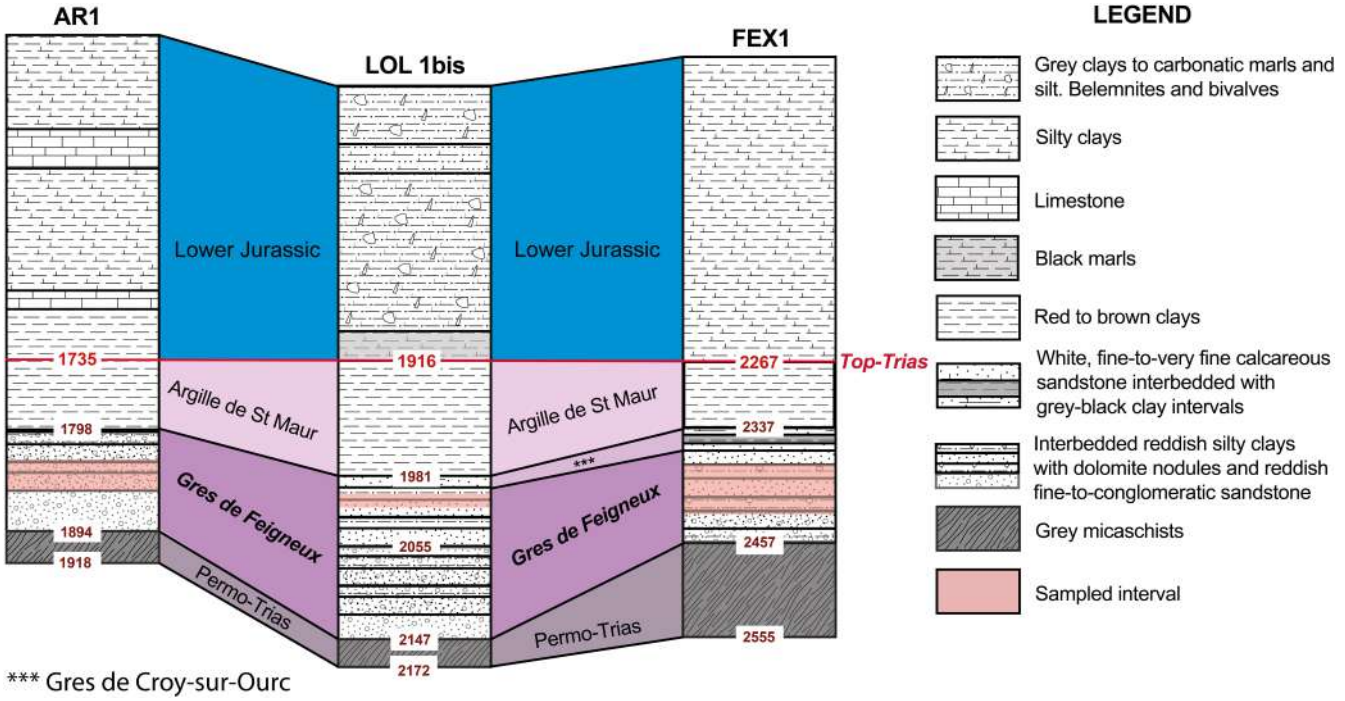

FIGURE 3 Well log stratigraphy of the three studied wells from Permo-Trias to Lower Jurassic. AR1, LOL1b and FEX1 stand respectively for Arsy 1, Longueil 1b and Feigneux 1 wells. The lithologies and stratigraphic interpretations are from the available well drilling reports. Grès de Feigneux corresponds to the local name for the Chaunoy Fm. The red line indicates the Upper Triassic – Lower Jurassic limit. The pink bands illustrate the sampled intervals from the three wells. Numbers along the stratigraphic columns refer to depths in meters.

as lacustrine carbonate mudstones and flood plain clay-rich facies (Figure 4c). They are frequently associated with subaerial or subaqueous debris-flow deposits mostly consisting of matrix-supported conglomerates (Figure 4d). Dolomite nodules developed within red clays (Figure 4e), typical of paleosoils, are also observed. For details on the sedimentary facies and depositional environments of the investigated samples see Appendix S1 (Data S1).

To apply different techniques to the diagenetic carbonates occurring in the sampled lithologies, rock slabs were produced from each sample to manufacture thin and thick sections for petrography and fluid inclusion (FI) studies and to sample carbonate powders for geochemical analyses.

3.2 | Petrographic analysis

Sixteen thin sections (50 μm thick) were prepared from rock slabs. They were partially stained with a solution of 10% diluted HCl, Alizarin red-S and potassium ferricyanide for carbonate identification and qualitative Fe content estimation (Dickson, 1966). Conventional optical petrography was performed with a Nikon ECLIPSE LV100 POL polarized light microscope, allowing observations under plane- and cross-polarized light (PPL and XPL). Calcite cement types and dolomite textures were described using the classifications from Flügel (2004) and Sibley and Gregg (1987), respectively. Cathodoluminescence (CL) microscopy supported petrographic analysis and was performed with a Nikon Eclipse ME600 polarized light microscope equipped with a CL 8200 Mk5 CITL apparatus operating under vacuum (<0.1 mBar) at 10 kV and 250 μA.

3.3 | O-C stable isotope analysis

A total of 24 diagenetic carbonates (18 calcites and 6 dolomites) were extracted with a dental drill (drill tip size of 0.5 mm) from rock slabs of 9 samples after petrographic analyses of mirror-like thin sections. The powders were reacted with 100% phosphoric acid at 70°C using a Gasbench II connected to a ThermoFisher Delta V Plus mass spectrometer and analysed for O and C stable isotopes. $\delta^{18}O$ and $\delta^{13}C$ values are reported in per mil (‰) relative to the Vienna Pee Dee Belemnite (VPDB) standard. Reproducibility and accuracy were checked by replicate analysis of laboratory standards calibrated by assigning $\delta^{13}C$ values of +1.95‰ to NBS19 and −47.3‰ to IAEA-CO9 and $\delta^{18}O$ values of −2.20‰ to NBS19 and −23.2‰ to NBS18. Reproducibility for

TABLE 1 Well of provenance, depth, facies and depositional environment of the studied samples from the Upper Triassic (Norian) Chaunoy Fm.

Well	Sample	Depth (m)	Facies	Depositional environment
Longueil 1b (LOL1b)	LOL 2003	2003.0	Carbonate mudstone	Lacustrine
	LOL 6-7	2006.5	Carbonate mudstone	Lacustrine
	LOL 2008	2008.0	Carbonate mudstone	Lacustrine
	LOL 2008b	2008.0	Carbonate mudstone	Lacustrine
	LOL 8-9	2008.5	Carbonate mudstone	Lacustrine
	LOL 8-9b	2008.5	Carbonate mudstone	Lacustrine
Arsy 1 (AR1)	AR1 17-18	1817.5	Clast-supported conglomerate	Lag deposits
	AR1 18-19	1818.5	Sandstone	Stream-flood and subacqueous channels
	AR1 8-9	1819.0	Red clay, dolomite nodules	Paleosoil
	AR1 5-6	1825.5	Clast-supported conglomerate	Lag deposits
Feigneux 1 (FEX1)	FEX 2370.8	2370.8	Clast-supported conglomerate	Lag deposits
	FEX 2371	2371.0	Matrix-supported conglomerate	Stream-flood and subacqueous channels
	FEX 2396	2396.0	Clast-supported conglomerate	Lag deposits
	FEX 2396b	2396.0	Clast-supported conglomerate	Lag deposits
	FEX 2405	2405.0	Matrix-supported conglomerate	Stream-flood and subacqueous channels
	FEX 8-7	2408.0	Sandstone	Stream-flood and subacqueous channels

$\delta^{13}C$ and $\delta^{18}O$ was ±0.07 and ±0.07 (1 SD), respectively. Oxygen isotope values of dolomite were corrected using phosphoric acid fractionation factors (Rosenbaum & Sheppard, 1986).

3.4 | Fluid inclusion (FI) study

Sample selection relied on the general limitations of the FI thermometry method which is mostly applied to burial diagenetic carbonates, characterized by clear colour, course crystallinity and presence of large (>3–5 μm) bi-phase FI with petrographic features suggesting a primary origin and the lack of post-entrapment modifications (Bodnar, 2003; Goldstein, 2001, 2003; Goldstein & Reynolds, 1994). Based on these requirements, eight double-polished thick sections (120 μm tick) were produced from the same rock slabs used for thin section production. The study comprised FI petrography followed by FI michrothermometry (FIM).

The apparatus used is a Linkam MDS 600 heating–freezing stage mounted on a Nikon ECLIPSE LV100 polarized light microscope, associated with a 100 W Mercury vapour lamp for UV-light observations. The Linksys 32 software enabled all the operations for FIM. The stage was calibrated with synthetic FI in quartz standards in the −21 to +135°C temperature range.

FI was ascribed, where possible, to Fluid Inclusion Assemblages (FIA) following the recommendations of Goldstein and Reynolds (1994) and Goldstein (2003). Size, shape, liquid/vapour ratio, and response under UV-light of the selected FI were determined at room temperature.

FIM analysis was executed in two different stages: (1) heating runs to determine homogenization temperatures (Th) and temperatures of gas nucleation after homogenization (Tn_g); (2) cooling runs to determine nucleation temperatures of ice-like phases (Tn_i), apparent eutectic temperatures (Te_{app}) and final melting temperatures of ice-like phases occurring with stable (Tm_i) and metastable

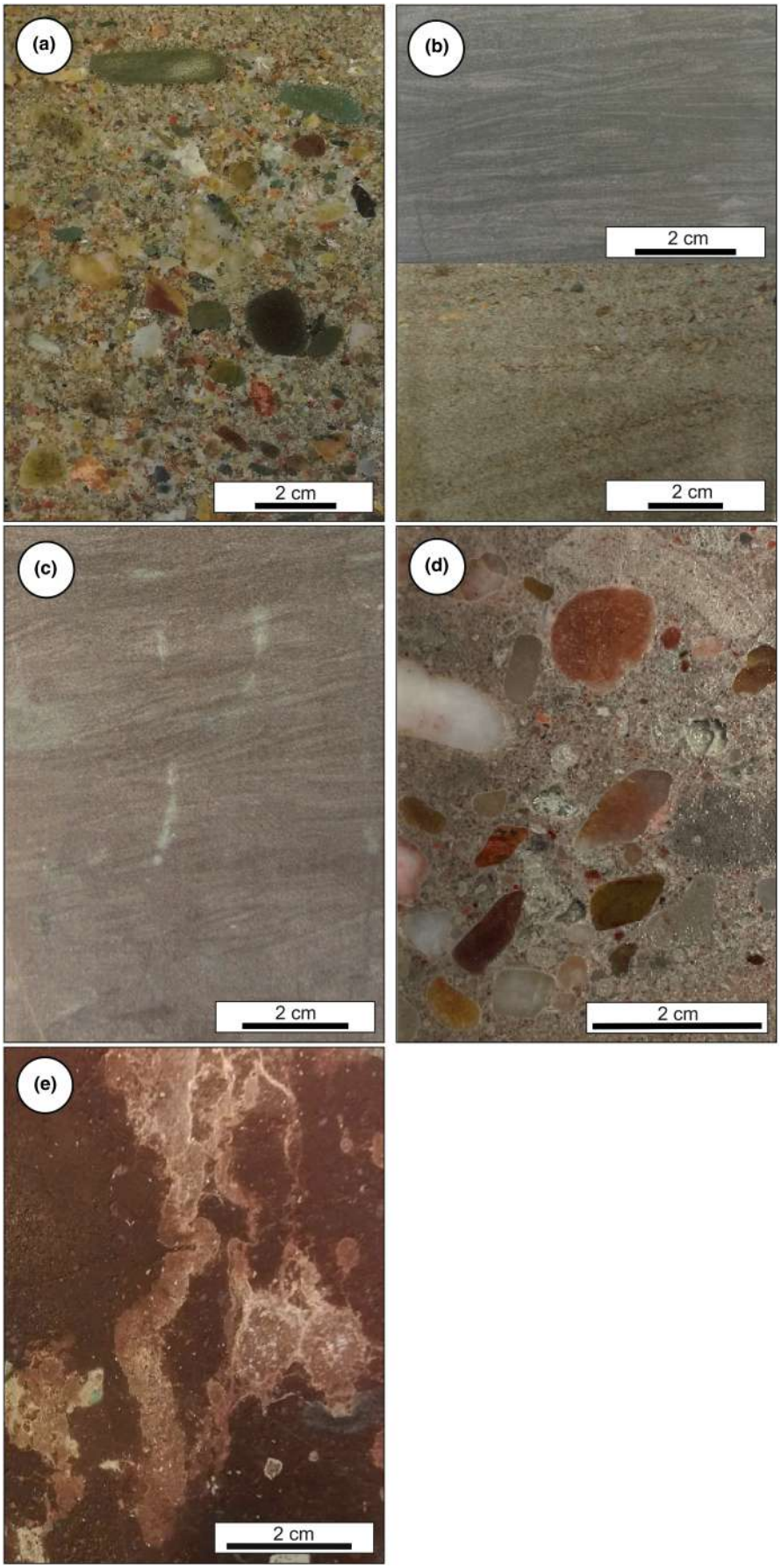

FIGURE 4 Main sedimentary facies observed in the studied samples from the Chaunoy Fm. (a) Clast-supported polygenic conglomerate, poorly sorted, ungraded to weakly graded. (b) Photo above: fine grained sandstone, well sorted, with trough cross-beds. Photo below: fine to coarse, moderately sorted and cross-bedded sandstone, composed of sub-angular to sub-rounded clasts. (c) Clay-rich facies composed of reddish clay laminae alternated with pinkish silstone and fine sandstone laminae. (d) Matrix-supported polygenic conglomerate, poorly sorted and ungraded. (e) Red clays with dolomitized root traces (paleosoil).

($Tm_{i(MET)}$) behaviour. Th and Tm_i measurements were accomplished with accuracy of ±1 to ±2°C and of ±0.1 to ±0.2°C, respectively. Salinities were calculated from stable Tm_i only in the binary H_2O-NaCl system (Bodnar, 1993) and are expressed as %wt. NaCl eq.

The software package FLUIDS (Bakker, 2003, 2009) was used to further characterize the aqueous fluids. The application BULK was employed to calculate bulk FI properties (e.g., density) using the equation of state of Krumgalz et al. (1996) and the measured Th and Tm_i. The program LONER32 was used to calculate isochore slopes, according to the thermodynamic model of Bodnar and Vityk (1994) and by using the measured Th and salinities.

3.5 | Carbonate clumped isotope (Δ_{47}) analysis

Sampling for Δ_{47} analysis was accomplished by giving priority to (1) the carbonate phases also analysed for FIM to discuss the results of the two thermal proxies (i.e. FIM vs. Δ_{47}); and (2) the most voluminous phases (i.e. the phases that occur at a spatial resolution higher than the 0.5 mm drill-points used for sampling), in order to avoid mixing between different carbonate generations occurring nearby. Based on these requirements, six diagenetic carbonate powders (ca. 2 mg) were extracted with a dental drill from rock slabs after petrographic analyses of mirror-like thin sections.

The clumped isotope compositions of carbonates were determined at the ETH Ziurich using a Thermo Fisher Scientific 253Plus mass spectrometer which is coupled to a Kiel IV carbonate preparation device, following the method described in Müller, Violay, et al. (2017). The Kiel IV device includes a custom-built PoraPakQ trap held at −40°C to eliminate potential organic contaminants. Prior to each sample run, the pressure-dependent backgrounds were determined on all beams to correct for non-linearity effects in the mass spectrometer. During each run, 18 replicates of 90–110 µg of different samples and 5 replicates of each of the three carbonate standards, ETH-1, ETH-2 and 10 replicates of the standard ETH-3 (Bernasconi et al., 2018, 2021), were analysed for data normalization. One replicate of the international standard IAEA C2 was analysed to monitor the long-term reproducibility of the method. Calcite was reacted for 7 min and 30 s and dolomite for 33 min to ensure a complete reaction. All instrumental and data corrections were carried out with the software Easotope (John & Bowen, 2016) using the revised IUPAC parameters for ^{17}O correction (Daëron et al., 2016). All clumped isotope values are reported in the I-CDES (Intercarb Carbon dioxide equilibrium scale) following the recommendations of Bernasconi et al. (2021).

Carbonate precipitation temperatures were calculated using the Anderson et al. (2021) calibration. This is the most robust calibration that resolved published discrepancies in previous calibrations which were due to poor standardization (Bernasconi et al., 2021).

The simultaneously measured $\delta^{18}O$ and $\delta^{13}C$ values were reported in per mil (‰) relative to the Vienna Pee Dee Belemnite (VPDB) standard.

3.6 | Δ_{47} solid-state reordering and reordering models

Clumped isotope temperatures of carbonate minerals that have undergone heating during burial have to be interpreted with caution due to the susceptibility of Δ_{47} compositions to undergo resetting by solid-state reordering (e.g., Hemingway & Henkes, 2021; Lawson et al., 2018; Lloyd et al., 2018; Mangenot et al., 2019; Passey & Henkes, 2012; Stolper & Eiler, 2015). The Δ_{47} solid-state reordering process is caused by diffusion and exchange of ^{13}C and ^{18}O isotopes which tend to reequilibrate with new ambient temperatures. It can occur without noticeable changes in the mineral bulk isotopic composition ($\delta^{13}C$, $\delta^{18}O$), elemental concentration, or texture (Dennis & Schrag, 2010; Henkes et al., 2014; Passey & Henkes, 2012). The reordering process chiefly depends on the temperatures experienced by the carbonate phases with time and on the residence time at each temperature step. Conversely, water presence, composition and pressure exert only modest influence on Δ_{47} reordering rates. Therefore, it is possible to make meaningful predictions about carbonate Δ_{47} reordering if a well-constrained thermal history is available, even when fluid composition and pressure are unknown (Brenner et al., 2018; Huntington & Petersen, 2023).

Modelling the Δ_{47} solid-state reordering during heating over time requires knowledge of the reordering kinetics and Arrhenius parameters of the mineral phases at issue, as well as on the temperature–time history they went through. Modelling outputs are known as thermal history reordering models (THRM, as defined by Shenton et al., 2015). Three models for carbonate Δ_{47} reordering exist: (1) the first-order reordering model from Passey and Henkes (2012); (2) the exchange-diffusion model from Stolper and Eiler (2015); and (3) the disordered kinetic model from Hemingway and Henkes (2021). The first model suggests that reordering occurs due to selective isotopic exchange during heating. This reordering process follows a first-order kinetic equation (Henkes et al., 2014; Passey & Henkes, 2012). The second model suggests that reordering is given both by an initial diffusion of isotopes through the crystal lattice followed by slow isotope

exchange reactions between adjacent carbonate groups (Stolper & Eiler, 2015). The third model suggests that reordering is the result of a random-walk ^{18}O diffusion through the carbonate lattice, occurring as a succession of first-order processes that take place simultaneously at different rates (Hemingway & Henkes, 2021). The first two reordering models (Passey & Henkes, 2012; Stolper & Eiler, 2015) can be treated as specific cases of the disordered kinetics, whereas the last model (Hemingway & Henkes, 2021) provides a generalized framework to constrain Δ_{47} reordering.

Both, the Passey and Henkes (2012) and the Stolper and Eiler (2015) reordering models are implemented within the ClumpyCool Python developed by Lloyd (2020) and available at https://github.com/maxmansaxman/Clumpy_reordering_model_distribution. The Hemingway and Henkes (2021) reordering model is implemented within the Isotopylog Python tool developed by Hemingway (2020) and is available at http://pypi.python.org/pypi/isotopylog.

4 | RESULTS

4.1 | Thin section petrography

Previous authors that studied Chaunoy Fm. samples from the basin depocenter reported the occurrence of different dolomite, calcite, quartz, and feldspar diagenetic phases (Worden & Matray, 1995, 1998). Conversely, in the studied samples no silicate diagenetic phases, such as quartz and feldspars were observed. Petrographic analysis of thin sections from the three investigated cores (LOL1b, AR1, FEX1; Figure 1) only allowed the identification of seven diagenetic carbonate phases and their relative chronology is illustrated in Figure 5 and described below.

In LOL1b well samples, a pervasive recrystallization is revealed by micrite crystal coarseness (>4 μm). The micrite occurring in FEX1 well samples displays hints of recrystallization as well, whereas no micrite is observed in AR1 well samples.

Three distinct dolomite phases (fDol, cDol, and eDol) are observed in samples from LOL1b and FEX1 wells. Based on their dominant petrographic feature these phases were named fine dolomite (fDol), coarser dolomite (cDol) and euheudral dolomite (eDol). They are followed by successive precipitation of calcite (Cal1 and Cal2) and dolomite (Dol1) phases.

fDol consists of a mosaic of fine crystals (<10 μm; dolomicrite) that make up a unimodal, nonplanar texture and display a dull brown CL (Figure 5a,b). It replaces the recrystallized micrite and may encrust microbial mats, locally observed in carbonate mudstone facies.

cDol is a fine to medium crystalline (25–50 μm) dolomite that post-dates fDol since it may replace or overgrow fDol crystals and is characterized by a bright red CL (Figure 5a,b).

eDol is constituted by a mosaic of euhedral (rhombohedral) crystals of variable coarseness (<100–500 μm) making up a polymodal, planar-E texture (Figure 5c) and locally displaying sweeping extinction. It usually exhibits a uniform bright red CL (Figure 5c). Less commonly the crystals are zoned and display dull brown cores with bright red external zones, occasionally, with bright orange rims. This phase replaces and therefore post-dates previous dolomites (cDol and fDol) or fills interparticle and vuggy pores.

Cal1 consists of non-ferroan blocky calcite crystals (400–2000 μm), characterized by a non-luminescent CL response, though they locally display a concentric CL zoning marked by thin bright orange rims (Figure 5b–f). This calcite phase mainly fills interparticle pores, vugs and fractures, though it locally replaces (and therefore post-dates) the cores of eDol crystals (Figure 5c). It is the most voluminous void-filling phase and occurs in samples from LOL1b and AR1 wells.

Cal2 consists of non-ferroan blocky calcite crystals (<400–1500 μm) which exhibit a uniform bright orange CL (Figure 5a–g). It post-dates Cal1 since it mainly forms overgrowths over Cal1 crystals and may fill interparticle pores, vugs and fractures (Figure 5e,f). Locally, it also replaces (and therefore post-dates) eDol crystals (Figure 5c). It mainly occurs in samples from AR1 and LOL1b wells and to a minor extent in FEX1 samples.

Dol1 consists of non-ferroan dolomite crystals (200–600 μm), making up a polymodal, nonplanar texture. The crystals display curved faces and a sweeping extinction, typical of saddle dolomite (Spötl & Pitman, 1998). This phase displays a uniform dull red CL (Figure 5g,h), mainly fills interparticle pores, vugs and fractures and forms overgrowths over Cal2 crystals (Figure 5h), therefore post-dating them. It occurs only in samples from FEX1 well.

4.2 | O-C stable isotope data

Oxygen and carbon stable isotope compositions of fDol ($n=2$), Cal1 ($n=13$), Cal2 ($n=5$) and Dol1 ($n=4$) are summarized in Table 2 and in Figure 6. The samples of fDol have $\delta^{18}O$ between −3.9‰ and −3.0‰ (mean: −3.5‰ ± 0.6‰) and $\delta^{13}C$ between −7.2‰ and −7.1‰ (mean: −7.2‰ ± 0.07‰). Cal1 samples have $\delta^{18}O$ between −7.2‰ and −3.8‰ (mean: −5.0‰ ± 1.0‰) and $\delta^{13}C$ between −7.7‰ and −6.6‰ (mean: −7.2‰ ± 0.3‰). Cal2 samples have $\delta^{18}O$ between −8.0‰ and −6.0‰

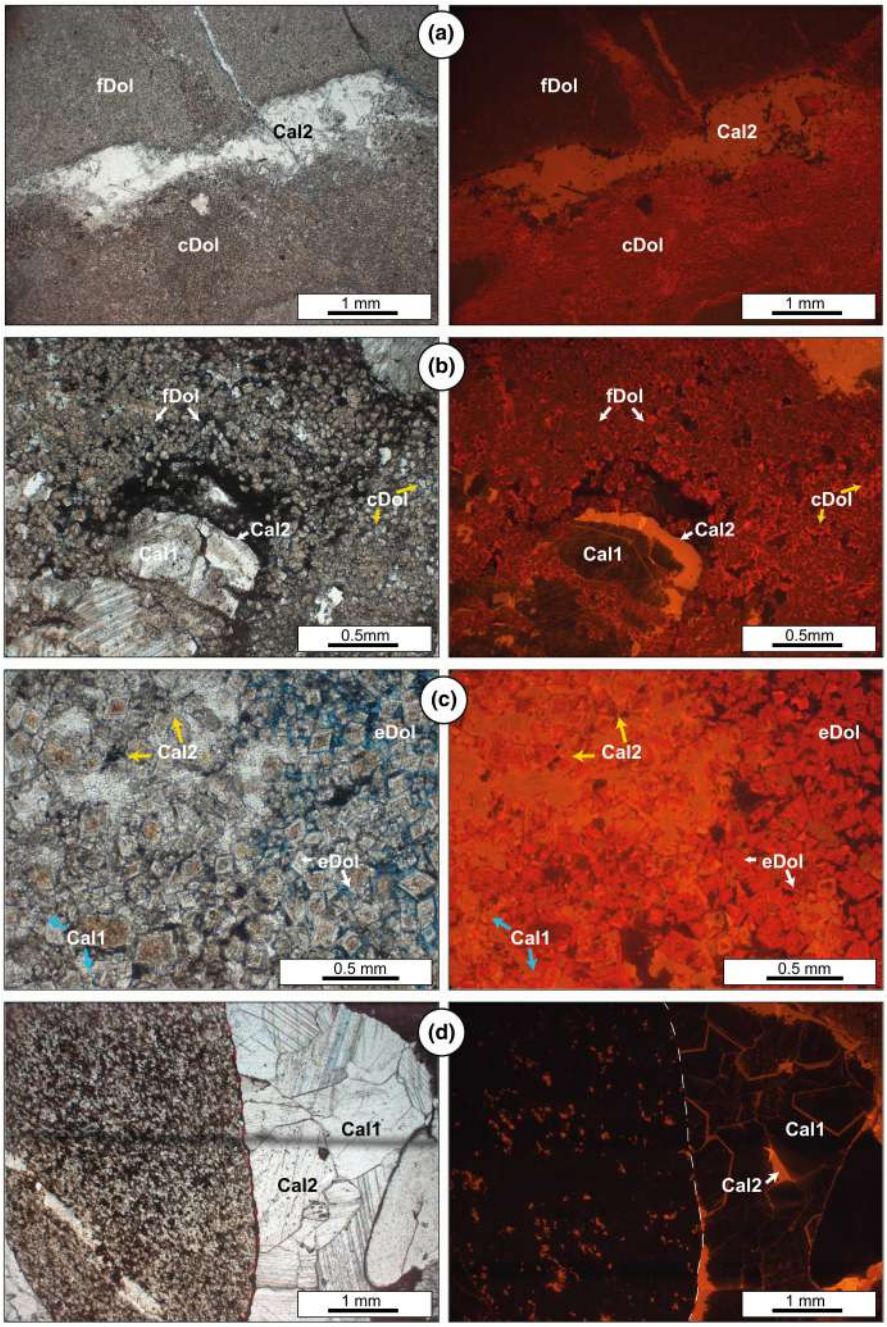

FIGURE 5 Microphotographs in plane-polarized light (to the left) and cathodoluminescence (CL; to the right) show the main petrographic features of the investigated diagenetic phases. (a) fDol dolomite, displaying a dull brown CL, pervasively replaces the preexisting micrite. It coexists with the bright red cDol dolomite. A vug occurring within the dolomite crystal mosaic is filled by later bright orange calcite cement (Cal2). Sample LOL 2003. (b) cDol dolomite displaying a bright red CL overgrowths fDol crystals (yellow arrows). A vug occurring within the dolomite crystal mosaic is filled by later non-luminescent and bright orange calcite cements (Cal1 and Cal2). Sample LOL 6-7. (c) Planar-E crystals of eDol dolomite displaying zoned CL with dull brown cores and bright red external zones. Some crystals are replaced by non-luminescent Cal1 (blue arrows) and bright orange Cal2 (yellow arrows). Sample LOL 8-9 (d) Cal1 blocky calcite crystals, displaying non-luminescent CL with thin bright orange rims, fill interparticle pores and are post-dated by bright orange Cal2. The dashed line demarcates a sandstone grain. Sample AR1 17-18. (e) Cal2 blocky calcite, displaying a uniform bright orange CL, forms thick overgrowths over the non-luminescent Cal1 and completely fills interparticle pores. Sample AR1 17-18. (f) Cal2 blocky calcite with uniform bright orange CL forms thin overgrowths over the non-luminescent Cal1 crystals. Sample LOL 6-7. (g) Dol1 saddle dolomite, displaying a dull red uniform CL completely fills interparticle pores. The dashed lines demarcate sandstone grains. Sample FEX 2396. (h) Cal2 with bright orange CL is overgrown by Dol1 with dull red CL, completely filling the remaining interparticle pore. Sample FEX 2370.8.

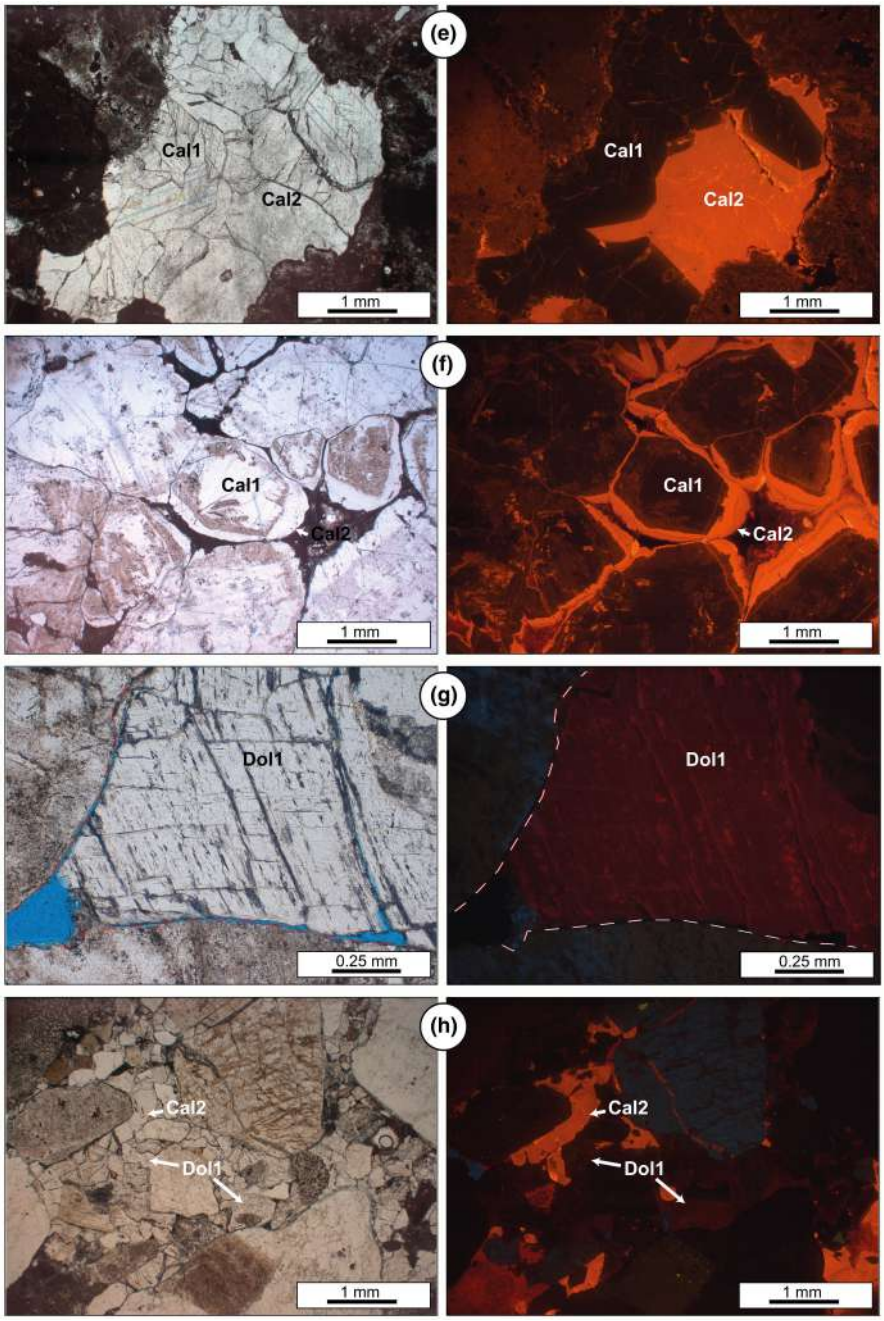

FIGURE 5 (Continued)

(mean: −6.9‰ ± 0.9‰) and $\delta^{13}C$ between −8.0‰ and −7.3‰ (mean: −7.6‰ ± 0.3‰). Finally, Dol1 samples have $\delta^{18}O$ between −11.0‰ and −10.3‰ (mean: −10.5‰ ± 0.3‰) and $\delta^{13}C$ between −7.7‰ and −7.3‰ (mean: −7.4‰ ± 0.2‰).

All investigated carbonate phases show consistently negative $\delta^{18}O$ and $\delta^{13}C$ values (Table 2; Figure 6). In particular, $\delta^{13}C$ values are very consistent among the different phases and vary between −8.0‰ and −6.6‰ (mean: −7.3‰ ± 0.3‰). Conversely, $\delta^{18}O$ values cover a large spread comprised between −11.0‰ and −3.0‰ with a progressive lower ^{18}O content going from fDol to Dol1.

4.3 | Fluid inclusion (FI) study

In the fDol, cDol and eDol dolomites FI could not be observed or were small (<2 μm) and only mono-phase liquid, this latter feature suggesting low trapping temperatures (<50°C; Goldstein & Reynolds, 1994). Conversely, the Cal1, Cal2 and Dol1 phases contained FI suitable for FIM

TABLE 2 Stable oxygen and carbon isotope compositions ($\delta^{18}O$, $\delta^{13}C$) for individual carbonate diagenetic phases investigated.

Sample	Phase	Mineralogy	CL response	$\delta^{18}O$ (‰, VPDB)	$\delta^{13}C$ (‰, VPDB)
LOL 2003	fDol	Dolomite	Dull brown	−3.0	−7.2
LOL 6–7	Cal1	Calcite	Non-luminiscent	−4.1	−7.2
	Cal1	Calcite	Non-luminiscent	−3.8	−6.6
LOL 2008	fDol	Dolomite	Dull brown	−3.9	−7.1
	Cal1	Calcite	Non-luminiscent	−4.6	−7.7
	Cal1	Calcite	Non-luminiscent	−4.2	−6.8
	Cal1	Calcite	Non-luminiscent	−4.2	−6.9
	Cal1	Calcite	Non-luminiscent	−6.3	−7.0
	Cal2	Calcite	Bright orange	−5.9	−7.8
LOL 8–9	Cal1	Calcite	Non-luminiscent	−4.9	−7.3
	Cal2	Calcite	Bright-orange	−6.2	−8.0
AR1 5–6	Cal1	Calcite	Non-luminiscent	−5.7	−7.4
	Cal2	Calcite	Bright orange	−6.8	−7.3
AR1 17–18	Cal1	Calcite	Non-luminiscent	−7.2	−7.5
	Cal1	Calcite	Non-luminiscent	−4.9	−7.5
	Cal1	Calcite	Non-luminiscent	−5.1	−7.5
AR1 18–19	Cal1	Calcite	Non-luminiscent	−5.3	−7.4
	Cal1	Calcite	Non-luminiscent	−5.1	−7.2
	Cal2	Calcite	Bright orange	−7.7	−7.4
	Cal2	Calcite	Bright orange	−7.9	−7.5
FEX 8–7	Dol1	Dolomite	Dull red	−10.4	−7.3
FEX 2396	Dol1	Dolomite	Dull red	−10.3	−7.3
	Dol1	Dolomite	Dull red	−10.3	−7.7
	Dol1	Dolomite	Dull red	−11.0	−7.3

Abbreviation: CL, cathodoluminescence.

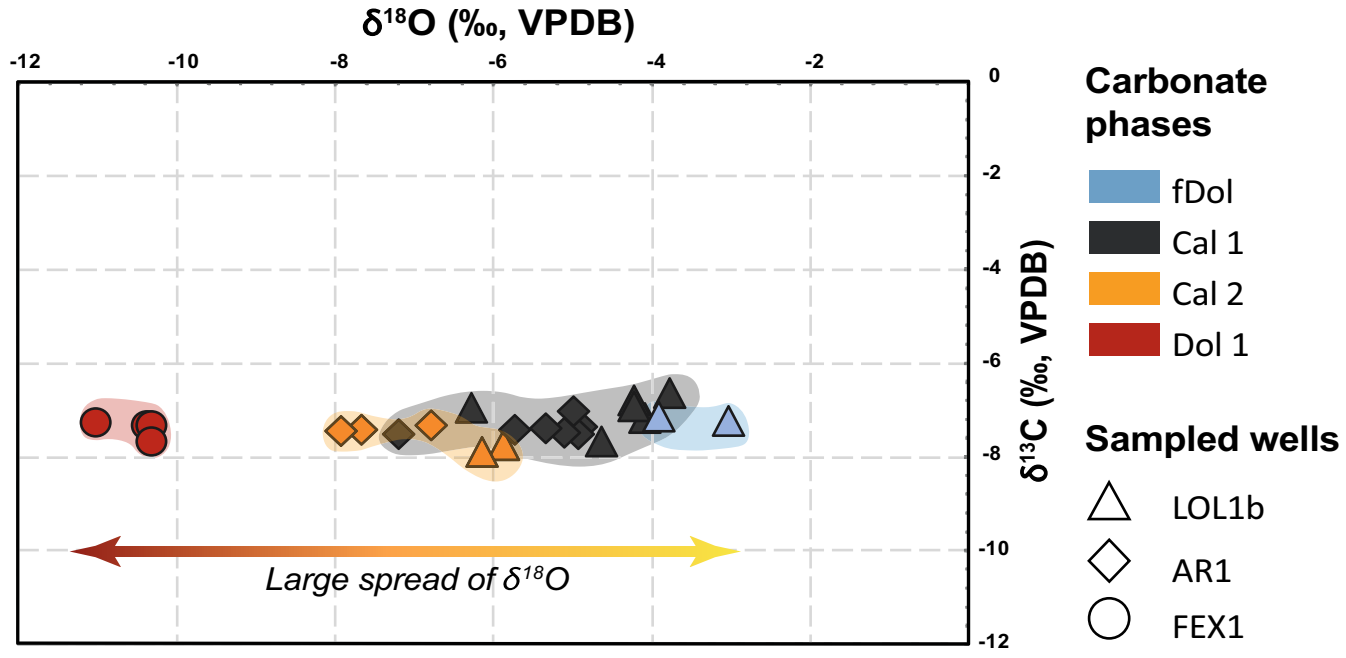

FIGURE 6 Stable oxygen and carbon isotope composition of the diagenetic carbonate phases. Dot colours refer to different phases, whereas dot shapes refer to the well of provenance. The coloured areas illustrate the dispersion of $\delta^{18}O$ and $\delta^{13}C$ values for each phase. Uncertainties are within the dot size.

measurements. Both mono-phase and bi-phase liquid FI were observed in these phases. Table 3 summarizes the main petrographic features of the bi-phase FI together with the corresponding microthermometry results. Details on petrography, microthermometry data and FI behaviour during microthermometry may be found in Appendix S1 (Table S1 and Data S2).

4.3.1 | FI petrography

The FI in Cal1, Cal2 and Dol1 do not show fluorescence under UV light, suggesting that they possibly contain aqueous fluids. No oil FI were ever observed in these diagenetic minerals, in line with the fact that the three investigated wells were barren.

Cal1 crystals contain mono-phase liquid FI, as well as bi-phase, liquid-rich FI. Both mono- and bi-phase FI commonly occur in growth zones (Figure 7a) or crystal cores and, less frequently, isolated. They have sizes mostly varying from 6 to 40 μm (Figure 7b) and display shapes from roundish to crystallographic controlled (e.g., squared, negative crystals), mimicking the crystallographic directions of the host crystal. Cal2 crystals contain mono- and bi-phase liquid-rich FI mostly occurring in crystal cores, growth zones, patches and locally isolated (Figure 7c,d). FI have sizes from 3 to 25 μm and shapes from roundish to crystallographic controlled (Figure 7d). Dol1 crystals only locally contain mono-phase FI. The most common bi-phase liquid-rich FI is up to 20 μm in size, occur mainly in crystal cores and growth zones and exhibit a dominant crystallographic controlled shape (Figure 7e,f).

The occurrence of FI in crystal cores and growth zones, together with the FI shapes controlled by host mineral crystallography (Figure 7), point to a possible primary origin of the mono- and bi-phase liquid-rich FI in Cal1, Cal2 and Dol1. Monophase FI was not further investigated since they cannot furnish the thermal information needed for this study. Conversely, bi-phase FI was further investigated with microthermometry.

4.3.2 | Fluid inclusion microthermometry (FIM)

During heating runs, total homogenization occurred in the liquid phase for all analysed bi-phase FI. During cooling runs ice melted last with both stable (Tm_i) and metastable behaviours ($Tm_{i(MET)}$). Further details on FI behaviour during microthermometry can be found in Appendix S1 (Data S2). Main microthermometry data

TABLE 3 Main results of the FI study (petrography and microthermometry) on Cal1, Cal2 and Dol1 carbonate phases.

Sample	Phase	FIA	Shape	Size	Homogenization temperature (Th)			Ice melting temperature (Tm_i)			Salinity		
				Range (μm)	Range (°C)	Mode (°C)	Mean (°C)	Range (°C)	Mode (°C)	Mean (°C)	Range (% wt. NaCl eq.)	Mode	Mean
LOL 2008	Cal1	G, I	CR, IR, EG	5–25	60–95	67.5	77.7 (19)	−16.0/−10.4	–	−12.3 (12)	14.4/19.4	–	16.2 (12)
	Cal2	G, P, I	IR, EG	3–15	70–100	84.0	83.4 (15)	−16.7/−10.6	−12.5	−13.5 (8)	14.6/20.0	16.4	17.3 (8)
LOL 8–9	Cal1	G	CR, IR	15–40	60–100	–	82.2 (19)	−15.8/−8.2	−11.8	−12.1 (13)	11.9/19.3	15.8	16.0 (13)
	Cal2	G, P	IR	10–25	85–110	88.5	94.5 (11)	−14.3/−10.2	−11.2	−16.0 (5)	14.15/18.0	15.2	15.9 (5)
AR1 18-19	Cal1	C, G	CR, IR	6–25	60–100	77.5	84.1 (29)	−12.3/−6.2	−9.8	−9.6 (14)	9.5/16.2	13.7	13.5 (14)
FEX 2396	Dol1	C, G	CR, IR	5–20	100–133	113.0	111.1 (20)	−17.3/−15.4	−16.3	−16.4 (11)	19.0/20.4	19.7	19.8 (11)

Note: Petrographic features of bi-phase FI at room temperature are shown together with range, mode and mean values of homogenization temperatures (Th), ice melting temperatures (Tm_i) and salinities calculated from Tm_i with the equation of Bodnar (1993). In parenthesis is reported the number of measurements for each parameter. Fluid Inclusion Assemblages: G, growth zone; C, crystal core; P, patches; I, isolated.FI shapes: crystallographic controlled (CR), irregular (IR), Elongated (EG). FI size is given as length in μm. Petrographic features of bi-phase FI at room temperature are shown together with range, mode and mean values of homogenization temperatures (Th), ice melting temperatures (Tm_i) and salinities calculated from Tm_i with the equation of Bodnar (1993). In parenthesis is reported the number of measurements for each parameter.

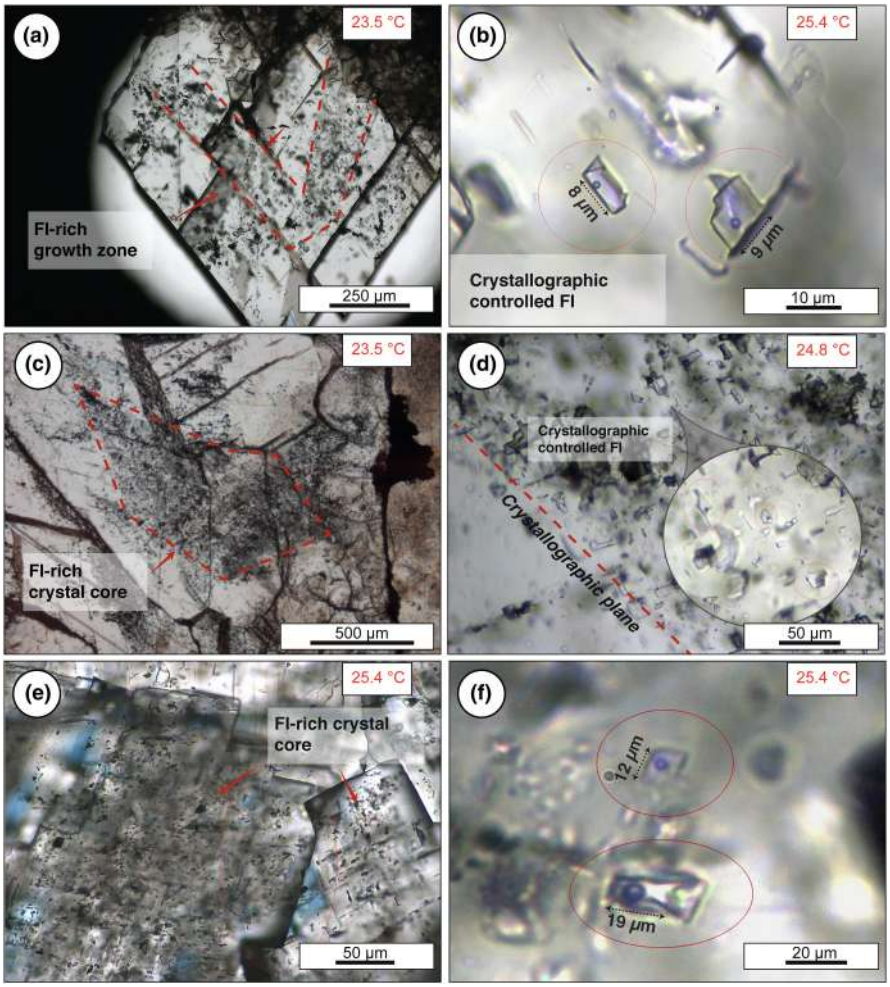

FIGURE 7 Photomicrographs showing some petrographic features of the FI in the investigated carbonate phases (Cal1, Cal2, Dol1). The temperatures at which the photos were taken are indicated in the red boxes. (a) Inclusion-rich growth zone in a Cal1 crystal. Sample LOL 2008. (b) Crystallographic controlled bi-phase liquid-rich FI in Cal1. (c) Inclusion-rich crystal cores of Cal2. Sample AR1 18-1. (d) FI-rich and FI-poor growth zones are separated by a crystallographic plane in Cal2. The zoom-in insert illustrates bi-phase liquid-rich FI with crystallographic controlled shapes. Sample AR1 18-19. (e) FI-rich crystal cores of Dol1. Sample FEX 2396. (f) Bi-phase liquid-rich FI in Dol1 with crystallographic controlled shapes. Sample FEX 2396.

from bi-phase FI of Cal1, Cal2 and Dol1 phases are reported in Table 3 and Th data are illustrated in Figure 8. In the text below we refer to calculated mode, which corresponds to the most frequent value among the individual temperatures (Th) measured in a sample and which does not represent the frequency intervals used for histogram calculation. FI in Cal1 samples homogenized in the range 60–100°C though most measured Th fall in the range 70–95C° (Table 3; Figure 8). The Th frequency histogram for LOL 2008 sample shows a bimodal distribution (Figure 8a) with calculated mode at 67.5°C. Th values for LOL 8-9 sample (Figure 8b) show a uniform and widespread distribution from 60 to 100°C, while Th in AR1 18-19 sample (Figure 8c) shows a normal Gaussian distribution with calculated mode at 77.5°C.

During reheating after freezing, a first melting was observed in the different Cal1 samples at temperatures (Te_{ap}) between −30 and −21°C. The Tm_i data recorded in Cal1 FI from LOL 2008 sample range from −16.0 to −10.4°C with an undefined mode and corresponding salinities included between 19.4 and 14.4%wt. NaCl eq. Tm_i from LOL 8-9 sample are between −15.8 to −8.2°C (mode = −11.8°C), with calculated salinities between 19.3 to 11.9%wt. NaCl eq. (mode = 15.8%wt. NaCl eq.). Tm_i in AR1 18-19 sample range from −12.3 to −6.2°C (mode = −9.8°C), with corresponding salinities between 16.2 and 9.5%wt. NaCl (mode = 13.7%wt. NaCl eq.). Recorded $Tm_{i(MET)}$ in the different Cal1 samples vary between −10.1 and −2.2°C.

FI from Cal2 samples homogenized in the range 70–110°C, though most measured Th fall in the range 80–90°C (Figure 8d,e). The Th frequency histograms show a

normal Gaussian distribution in LOL 2008 sample (Figure 8d) with calculated mode at 84.0°C and a right-skewed distribution in LOL 8-9 sample with calculated mode at 88.5°C (Figure 8e).

A first melting for Cal2 FI was observed in the two investigated samples at temperatures (Te_{ap}) between −30 to −26. The Tm_i data are rather consistent. In LOL 2008 sample Tm_i ranged from −16.7 to −10.6°C (mode = −12.5°C) with corresponding salinities between 20.0 and 14.6 %wt. NaCl eq. (mode = 16.4 %wt. NaCl eq.). In LOL 8-9, sample Tm_i is included between −14.3 and −10.2°C (mode = −11.2°C) with corresponding salinities included between 18.0 and 14.15 %wt. NaCl eq. (mode = 15.2 %wt. NaCl eq.). $Tm_{i(MET)}$ values recorded in the different Cal1 samples are from −9.5 to −2.5°C.

Te_{ap} values for FI from Cal1 and Cal2, comprised between −21 to −30°C, suggest that fluids are dominated by NaCl though other salts may be present (Goldstein & Reynolds, 1994).

FI from the Dol1 sample homogenized between 100 and 133°C though most of the measured Th fall in the range 100–115°C (Figure 8f). The Th frequency histogram shows a bimodal distribution with calculated mode at 113.0°C (Figure 8f).

Tm_i values in Dol1 FI range from −17.3 to −15.4°C (mode = −16.3°C), with calculated salinities going from 20.4 to 19.0 %wt. NaCl eq. (mode = 19.7 %wt. NaCl eq.). $Tm_{i(MET)}$ values were recorded from −18.9 to −12.6°C.

4.4 | Clumped isotopes (Δ_{47})

The fDol, cDol and eDol dolomites were not sampled for Δ_{47} analyses since they did not meet the requirements previously established (see Section 3.5). Conversely, 6 carbonate phases suitable for Δ_{47} analyses were sampled from Cal1, Cal2 and Dol1.

Table 4 summarizes $\delta^{18}O$, $\delta^{13}C$ and $T(\Delta_{47})$values obtained through clumped isotope (Δ_{47}) analysis on Cal1 ($n = 3$), Cal2 ($n = 2$) and Dol1 ($n = 1$) samples. Uncertainties calculated from 7 to 15 replicates are reported at the 95% confidence level, as suggested by Müller, Fernandez, et al. (2017) and Fernandez et al. (2017). In Figure 8, $T(\Delta_{47})$ data are reported together with Th from FIM acquired on the same carbonate phases. Full Δ_{47} data collected for the different samples may be found in Appendix S1 (Tables S2 and S3).

The three Cal 1 samples have $\delta^{18}O$ between −5.8‰ and −4.7‰ (mean = −5.4‰ ± 0.6‰), and a $\delta^{13}C$ between −7.5‰ and −7.2‰ (mean = −7.4‰ ± 0.2‰). The $T(\Delta_{47})$ values are: 51 ± 7.5°C ($n_r = 17$), 59 ± 8.0°C ($n_r = 15$) and 72 ± 7.9°C ($n_r = 16$), with a mean of 61 ± 8°C (Figure 8; Table 4). The two Cal 2 samples have $\delta^{18}O$ included

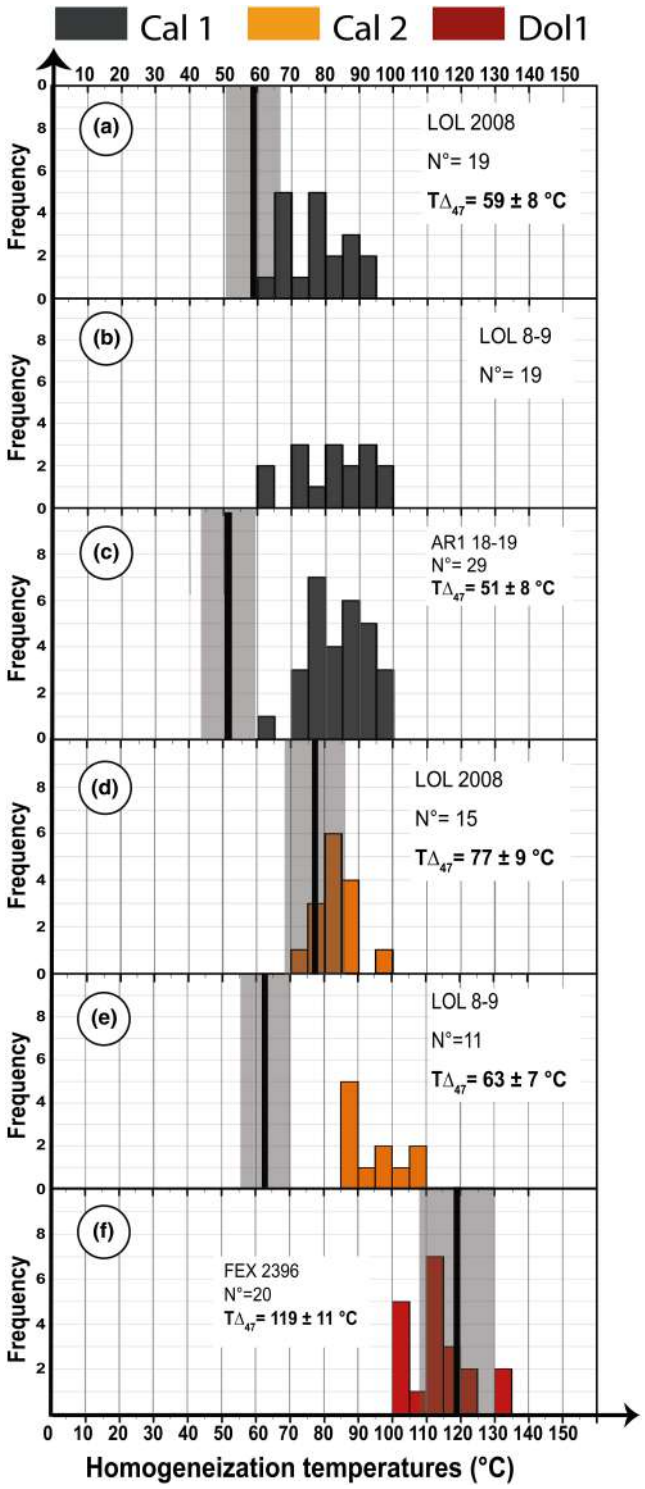

FIGURE 8 Frequency histograms of FI homogenization temperatures (Th) for Cal1, Cal2 and Dol1 samples. N° stands for the number of Th measured for each sample. For comparison, the $T(\Delta_{47})$ measured on the same samples is represented by black/grey bars. The width of the bars represents the $T(\Delta_{47})$ uncertainties reported at the 95% confidence level. (a–c) Cal1 blocky calcite from LOL 2008, LOL 8-9 and AR1 18-19 samples, respectively. (d, e) Cal2 blocky calcite from LOL 2008 and LOL 8-9 samples, respectively. (f) Dol1 saddle dolomite from FEX 2396 sample.

Sample	Phase	n_r	$\delta^{18}O$ (‰, VPDB)	$\delta^{13}C$ (‰, VPDB)	Δ_{47} (I-CDES) (‰)	$T\Delta_{47}$ (°C)
LOL 2008	Cal1*	15	−4.68 ± 0.03	−7.19 ± 0.02	0.510 ± 0.031	59 ± 8.0
	Cal2*	18	−8.40 ± 0.12	−8.02 ± 0.02	0.475 ± 0.034	77 ± 9.4
LOL 8-9	Cal2*	17	−6.94 ± 0.33	−7.98 ± 0.14	0.501 ± 0.026	63 ± 6.6
AR1 18-19	Cal1*	17	−5.67 ± 0.07	−7.49 ± 0.04	0.527 ± 0.033	51 ± 7.5
AR1 17-18	Cal1	16	−5.80 ± 0.08	−7.50 ± 0.04	0.483 ± 0.028	72 ± 7.9
FEX 2396	Dol1*	16	−10.31 ± 0.24	−7.40 ± 0.11	0.411 ± 0.029	119 ± 11.4

Note: Five out of the six carbonate phases (indicated by asterisks) were investigated also for FIM.

Abbreviations: Δ_{47}(I-CDES), Intercarb-Carbon Dioxide Equilibrium Scale (Bernasconi et al., 2021); n_r, number of replicates per sample; T(Δ_{47}), temperatures derived from the Anderson et al. (2021) calibration.

TABLE 4 Stable isotope ($\delta^{18}O$, $\delta^{13}C$, Δ_{47}) compositions of Cal1, Cal2 and Dol1 from clumped isotope analysis are reported at the 95% confidence level.

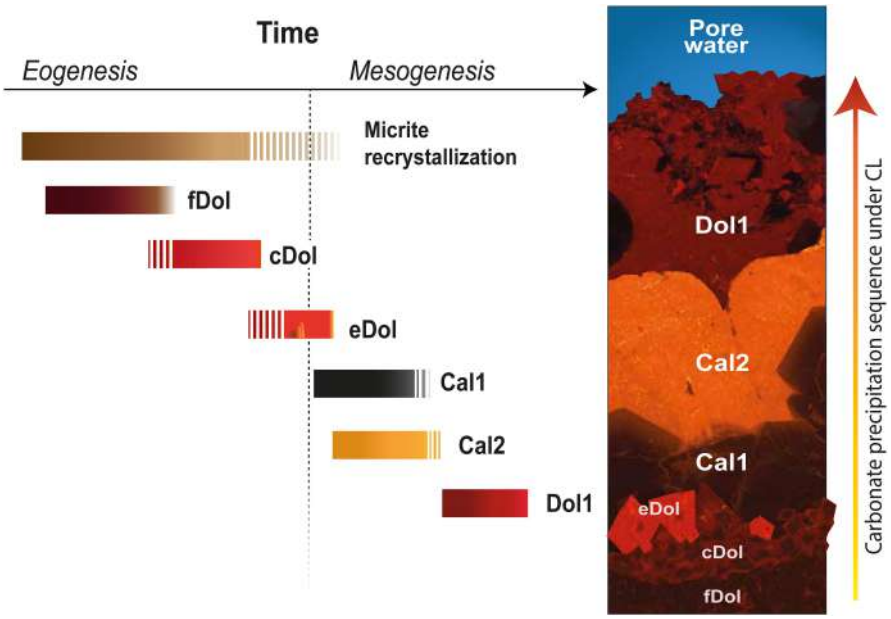

FIGURE 9 Paragenesis of carbonate precipitation events, in the Chaunoy Fm. samples. To the right, a schematic representation of the carbonate precipitation sequence as observed under CL.

between −8.4‰ and −6.9‰ (mean = −7.7‰ ± 1.0‰), and $\delta^{13}C$ of −8.0‰. The T(Δ_{47}) values are respectively 77 ± 9.4°C (n_r = 18; Figure 8d) and 63 ± 6.6°C (n_r = 17; Figure 8e) with a mean of 70 ± 8°C. Dol1 sample has $\delta^{18}O$ of −10.3‰, $\delta^{13}C$ of −7.4‰ and T(Δ_{47}) of 119 ± 11°C (n_r = 16; Figure 8f).

5 | DISCUSSION

5.1 | Carbonate precipitation sequence

The relatively fine crystallinity, common euhedral texture and lack of bi-phase FI of fDol, cDol and eDol (see Sections 4.1 and 4.3) suggest that these phases possibly precipitated during early diagenesis and surely at temperatures <50°C (Goldstein & Reynolds, 1994; Sibley & Gregg, 1987). Conversely the isotope and FI data (see Sections 4.2–4.4) suggest that Cal 1, Cal2 and Dol1 precipitated at higher temperatures. Based on these information and on the cross-cutting relationships among the observed diagenetic carbonate phases (see Section 4.1 and Figure 5) a possible precipitation sequence (paragenesis) was reconstructed (Figure 9). Accordingly, fDol and cDol were ascribed to early diagenesis (eogenesis), whereas Cal1, Cal2 and Dol1 were ascribed to burial diagenesis (mesogenesis). At the transition between eogenesis and mesogenesis was located eDol locally displaying sweeping extinction, a typical feature of dolomites precipitated during burial (Spötl & Pitman, 1998).

The focus of this contribution is the study of carbonate phases that precipitated during burial diagenesis (mesogenesis) since earlier diagenetic phases could not be investigated with fluid inclusion microthermometry. Specifically, this study focused on Cal1, Cal2 and Dol1 that could be investigated by both FI and Δ_{47} thermometry. The relative precipitation order (Figure 9) was based on: (1) the observation of rhombohedral eDol being partially

to totally replaced by Cal1 and Cal2 (Figure 5c); (2) the common occurrence of Cal2 as overgrowths on Cal1 crystals (Figure 5b–f); (3) the observation of Dol1 growing on Cal2 crystals or occurring as the last void-filling phase (Figure 5g,h).

Fluid inclusion and geochemical data support the petrography-based paragenetic sequence (Figure 9). The $\delta^{18}O$ values of Cal1, Cal2 and Dol1 span from −3.8‰ to −11.0‰ and globally become more negative going from Cal1 to Dol1 (Figure 6; Table 2). Furthermore, FIM analysis indicates increasing Th and salinity for Cal1, Cal2 and Dol1 parent fluids (Figures 8 and 10) and Δ_{47} analysis points at increasing $T(\Delta_{47})$ from Cal1 to Dol1 (Table 4; Figure 8). The discrepancies observed between temperatures recorded by FIM and Δ_{47} analyses (Figure 8) will be discussed in the following sections.

5.2 | FI trapping temperatures and thermal reequilibration

The main assumption needed to confidently apply FIM is that the FI behaved as isochoric and closed systems through time (Goldstein & Reynolds, 1994; Roedder & Bodnar, 1980). Several processes are known to induce FI post-entrapment modifications, undermining these assumptions. FI which experience temperatures higher than those of trapping or which undergo uplift on a different isochore may undergo internal pressure increase (Bodnar, 2003; Goldstein, 2001). Such process, referred as thermal reequilibration, may induce stretching or leakage and refilling of some FI. Stretching leads to FI volume increase (and density decrease) that results in Th overestimating the original temperatures of liquid–gas homogenization and in erroneous evaluation of trapping temperatures (Tt). Diversely, leakage and refilling imply that FI open to ambient pore fluids that may be sealed within the FI cavity, resulting in modification of the original salinities. Thermal reequilibration commonly affects carbonates which are relatively soft minerals. Therefore, the use of carbonates to infer thermo-barometric and compositional conditions of fluid-flow events in sedimentary basins requires evaluating thermal reequilibration occurrence.

To account for thermal reequilibration in FI from Cal1, Cal2 and Dol1 the criterium based on the FIA approach was used. This criterion states that if 90% of the inclusions from the same FIA have Th within a ±10°C range, the thermal data may be considered consistent, and the inclusions possibly did not experience thermal reequilibration (Goldstein & Reynolds, 1994).

The Th datasets obtained for each sample reveal not to be fully consistent, since only 70%–80% of the Th measured within individual FIA fall in a range of ±10°C (see Table S1). Conversely, Tm_i data from the same samples reveal to be relatively consistent, and the salinities calculated for individual samples vary from 1 to 5 wt.% NaCl eq. at most (see Table 3 and also in Table S1). This means that at least some of the primary FI trapped in Cal1 and Cal2 and to a minor extent also in Dol1 were affected by stretching, though they escaped leakage and refill, therefore preserving the original fluid composition. FI that has behaved like closed though not isochoric systems through time may be used to apply a pressure correction and to determine FI trapping temperatures and pressures (Tt and Pt), considering the minimum Th as the best estimate of the true homogenization (Goldstein, 2001; Goldstein & Reynolds, 1994).

The determination of Tt and Pt requires knowledge of FI density and a geologically coherent thermo-barometric gradient. Bulk fluid densities were determined from FI salinity mode values and are 1.066–1.092 g/cm^3 for Cal1, 1.062–1.086 g/cm^3 for Cal2 and

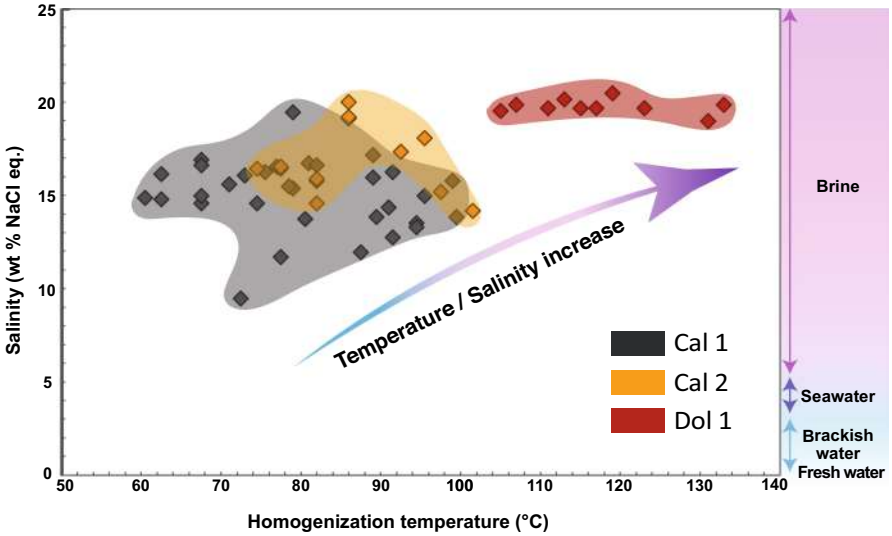

FIGURE 10 Homogenization temperature versus salinity cross-plot for FI from Cal1, Cal2 and Dol1 phases.

1.098 g/cm^3 for Dol1. A mean surface temperature of 20°C and a geothermal gradient of 35°C/km, which possibly characterized the Paris Basin in Mesozoic times (Torelli et al., 2020; Worden et al., 1999), were used together with a hydrostatic geobarometric gradient of 10 MPa/km, in line with the lack of major overpressure during the geological evolution of the studied reservoirs (Gonçalvès et al., 2010). Accordingly, Tt and Pt were estimated for FI within the different samples (Figure 11). The three Cal1 samples reveal consistent Tt and Pt of 64°C and 13 MPa, whereas the two Cal2 samples have Tt and Pt respectively of 76/93°C and 16/21 MPa. Finally, Dol1 sample has Tt and Pt of 110°C and 26 MPa.

5.3 | Clumped isotope temperature and solid-state reordering

Provided a well-constrained thermal history, the three existing Δ_{47} reordering models (Hemingway & Henkes, 2021; Passey & Henkes, 2012; Stolper & Eiler, 2015), introduced in Section 3.6, may be used to assess if the analysed carbonates preserved the pristine Δ_{47} compositions or if they underwent reordering and to which extent (e.g. Gasparrini et al., 2023; Mangenot et al., 2019; Naylor et al., 2019).

The temperature–time history experienced by the samples investigated in this study can be derived from the most updated 3D numerical basin model of the Paris Basin, available under TemisFlow™ software (Torelli et al., 2020; see Section 2.2). According to this model, the Upper Triassic (Norian) succession from the three studied wells (LOL1b, AR1 and FEX1) experienced a similar burial and thermal history. This is consistent with the wells being located <20 km apart and with the overlying Toarcian organic-rich deposits falling within the same Rock-Eval maturity zone (Tmax mostly 430–435°C; Delmas et al., 2002). Accordingly, the evolution of the Norian succession was characterized by progressive burial and heating during the Mesozoic and was followed by uplift and cooling during the whole Tertiary. The thermal maximum was reached during Late Cretaceous and persisted for ca. 20 My. More specifically, the maximum burial, thermal maximum and bottom hole temperatures for the studied Norian succession are: (1) 2.9 km, 110 and 84°C in LOL1b well; (2) 2.7 km, 102 and 74°C in AR1 well; (3) 3.0 km, 115 and 95°C in FEX1 well.

To explore the Δ_{47} reordering of Cal1 and Cal2 the thermal history from LOL1b well was integrated into the three existing reordering models (Hemingway & Henkes, 2021; Passey & Henkes, 2012; Stolper & Eiler, 2015), using the different Phyton numerical codes available (Hemingway, 2020; Lloyd, 2020; see Section 3.6). Results of the different modelling runs may be found in the Appendix S1 (Table S4).

By considering a calcite precipitated at temperatures as low as 30°C, assumed as the minimum precipitation temperature for a burial calcite, the models of Hemingway and Henkes (2021) and Passey and Henkes (2012) predict no change in the calcite Δ_{47} composition through reordering (Figure 12a). Any calcite precipitated at temperatures >30°C, and suffering the same thermal history would be less exposed to reordering. It results that Cal1 and Cal2 did not experience reordering and the measured T(Δ_{47}) (Figure 8; Table 4) reflect pristine precipitation temperatures.

In contrast, the model of Stolper and Eiler (2015) suggests that Cal1 and Cal2 have undergone reordering, resulting in measured TΔ_{47} higher than true precipitation temperatures (i.e. apparent T(Δ_{47})). We back-calculated the most probable precipitation temperatures for Cal1 and Cal2 by considering this reordering model, the measured

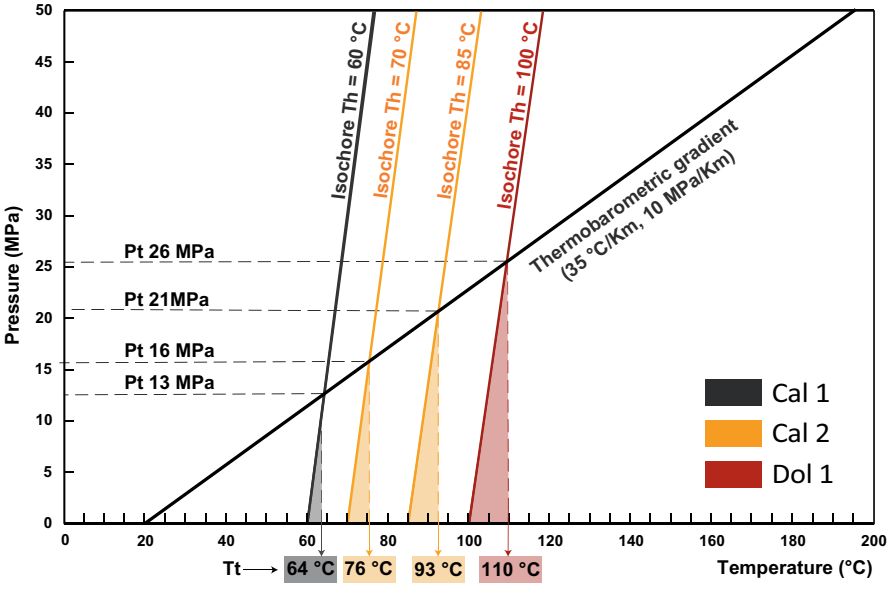

FIGURE 11 Trapping temperature (Tt) and trapping pressure (Pt) of FI in Cal1, Cal2 and Dol1. Thermo-barometric geothermal gradient: 35°C/km and 10 MPa/km in hydrostatic conditions; surface temperature: 20°C.

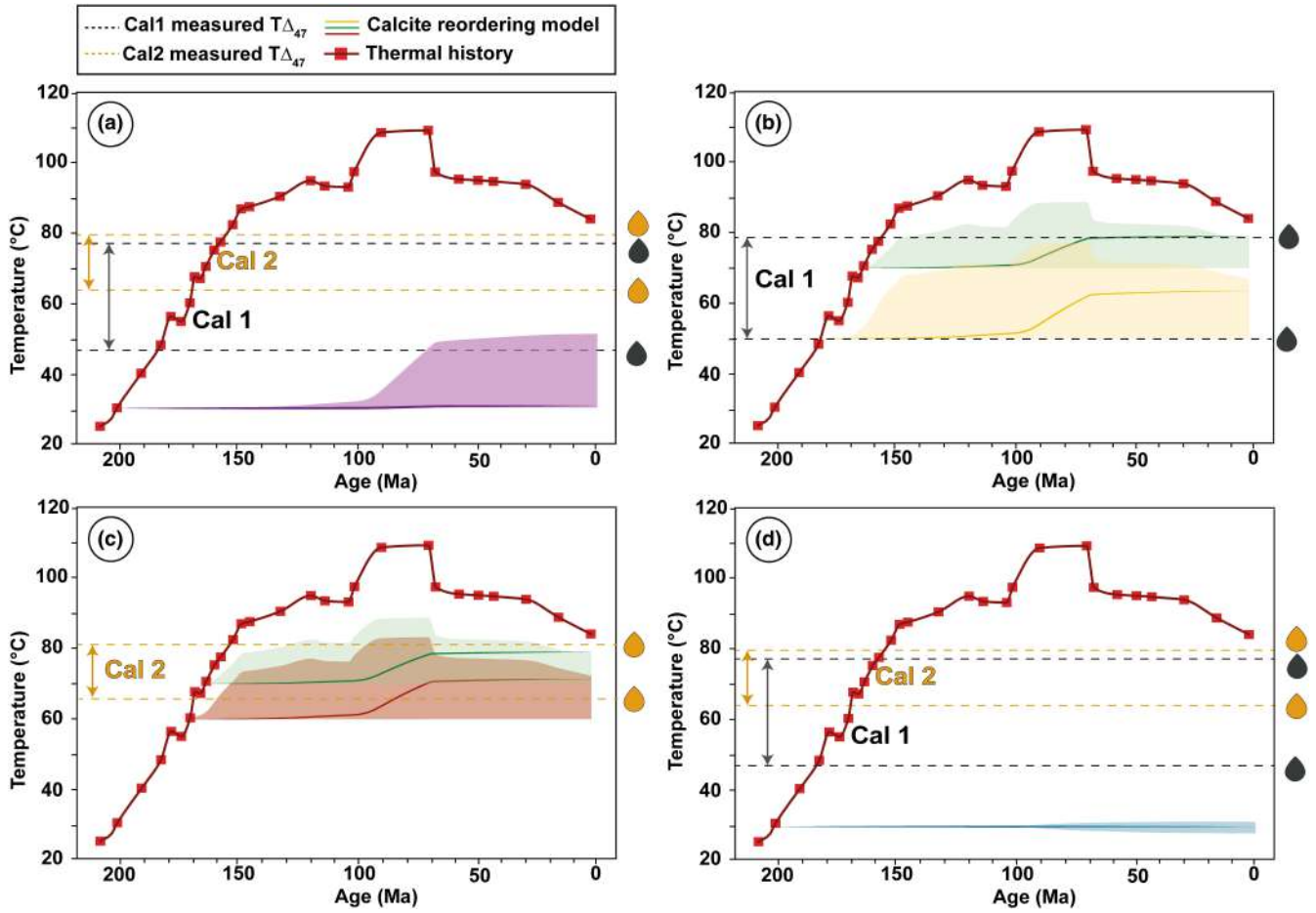

FIGURE 12 Modelling of the reordering behaviour of calcite T(Δ_{47}) using different reordering models, compared with the TΔ_{47} measured for Cal1 and Cal2. Shaded areas correspond to 2σ uncertainties at the output of the model. The black and orange dashed lines indicate the range of apparent T(Δ_{47}) measured for Cal1 and Cal2, respectively. The red lines represent the 1D thermal curve for the Upper Triassic (Norian) succession extracted from the available basin thermal model under TemisFlow™ (Torelli et al., 2020). (a) Predictions from the Passey and Henkes (2012) model for a calcite precipitated at 30 C. (b) Predictions from the Stolper and Eiler (2015) model for hypothetical calcite precipitation temperatures of 50 and 70°C, matching the T(Δ_{47}) measured for Cal1. (c) Predictions from the Stolper and Eiler (2015) model for hypothetical calcite precipitation temperatures of 60 and 70°C, matching with the T(Δ_{47}) measured for Cal2. (d) Predictions from the Hemingway and Henkes (2021) model for hypothetical calcite precipitated at 30°C.

TΔ_{47} and the thermal history suffered by the samples, using an approach previously implemented by Lawson et al. (2018). We modelled how the Δ_{47} composition of calcites precipitated at different hypothetical temperatures (comprised between 30 and 80°C) would have evolved given their thermal history and with a 2σ uncertainty at the output of the model. For each hypothetical precipitation temperature, a reordering pathway was modelled, illustrating the final T(Δ_{47}) that calcite would have acquired due to solid-state reordering (Figure 12b,c). The final T(Δ_{47}) modelled for each hypothetical precipitation temperature was compared with the apparent T(Δ_{47}) measured for Cal1 and Cal2, allowing to link the apparent T(Δ_{47}) back to their original precipitation temperature. Accordingly, the most probable precipitation temperatures for Cal 1 and Cal2 were estimated to be 50–70 and 60–70°C, respectively (Figure 12b,c).

Dolomite is known to be more resistant than calcite to reordering, so that more severe thermal conditions are needed for Δ_{47} to be reset (Ferry et al., 2011; Lloyd et al., 2017, 2018; Ryb et al., 2017). Indeed, all the three models used do not predict Δ_{47} reordering for dolomites precipitated at temperatures as low as 30°C and having experienced the most severe thermal history of FEX1 well, in which Dol1 occurs. More generally, the model of Passey and Henkes (2012) predicts complete reordering of dolomite Δ_{47} when temperatures of 180°C are reached and persist for tens of My, whereas the model of Stolper and Eiler (2015) predicts partial reordering of dolomite Δ_{47} from 150°C. The most recent reordering model of Hemingway and Henkes (2021) predicts that complete reordering only occurs at temperatures above ca. 280°C after 100 My. All these temperature thresholds are significantly higher than: (1) the thermal maximum of ca. 115°C experienced

by the studied samples in the FEX1 well, and (2) the $T(\Delta_{47})$ measured for Dol1 (Figure 8; Table 4). Therefore, we can conclude that the $T(\Delta_{47})$ derived for Dol1 reflects the pristine dolomite precipitation conditions.

5.4 | Precipitation timing and $\delta^{18}O_{fluid}$: FIM versus Δ_{47}

Advances in LA-ICP-MS technique allows at present to achieve in situ absolute dating of low U-bearing carbonate minerals by U-Pb geochronology (Gasparrini et al., 2023; Lawson et al., 2018; Mangenot, Gasparrini, Gerdes, et al., 2018; Montano et al., 2021, 2022; Roberts et al., 2020). U-Pb dating via LA-ICP-MS was attempted for the investigated carbonate phases (see Data S3 in Appendix S1). The analyses revealed to be unsuccessful due to high common Pb and low U contents of the carbonates. In absence of absolute radiometric dating of carbonate phases, diagenesis studies conventionally combine basin thermal histories and carbonate thermometric data to infer the carbonate precipitation timing. This indirect approach to "date" diagenetic mineralizations and fluid-flow events is a common practice in basin analysis that requires a well-framed basin thermal history to be applied (Gasparrini et al., 2021, 2023; Ronchi et al., 2011; Tournier et al., 2010). On the other hand, thermometric data from carbonate diagenetic phases may also be used to calculate the oxygen isotope compositions of the mineralizing fluids ($\delta^{18}O_{fluid}$), by using well established carbonate-water fractionation equations (e.g. Horita, 2014; O'Neil et al., 1969) with the aim of inferring possible fluid sources (e.g. Gabellone et al., 2013; Gasparrini et al., 2013; Swart, 2015; Van Geldern et al., 2013).

In this study we can rely on a robust basin thermal model (Torelli et al., 2020; see details in Section 2.2), on precipitation temperatures for Cal1, Cal2 and Dol1 phases based on FIM and Δ_{47} analyses and on carbonate $\delta^{18}O$ values independently measured for the same phases. Therefore, the carbonate precipitation temperatures can be plotted on the thermal curve of the studied succession, converted into precipitation timing and used to constrain $\delta^{18}O_{fluid}$ compositions. To do this, it must be assumed that precipitation of the studied carbonates occurred from fluids in equilibrium with the ambient rocks. This sounds to be a realistic scenario, since only few hydrothermal phases have been locally described from the Paris Basin, and exclusively in Jurassic successions from the depocenter and the eastern margin (Brigaud et al., 2020; Mangenot, Gasparrini, Gerdes, et al., 2018).

The final aim here is to use the different thermometric data (i.e., Th/Tt, $T(\Delta_{47})$) obtained from FIM and Δ_{47} (see Sections 5.2 and 5.3) to draw possible scenarios for the origin of the carbonate phases (Figure 13). The different precipitation temperatures for Cal1, Cal2 and Dol1 were plotted (with their uncertainties, where applicable) on the thermal curves (extracted from the model of Torelli et al., 2020) of the wells wherefrom the carbonate phases were analysed to determine the possible carbonate precipitation timing. In parallel, the $\delta^{18}O_{fluid}$ compositions, expressed in per mil (‰) relative to the Standard Mean Oceanic Water (SMOW), were calculated by using the fractionation equations of Horita (2014) and O'Neil et al. (1969) for calcite and dolomite samples, respectively.

The first scenario is based on FIM data (Table 3; Figure 13a). Some FI in Cal1, Cal2 and Dol1 show hints of thermal reequilibration so that trapping temperatures (Tt) were calculated from minimum Th (Figure 11). The derived precipitation ages are between ca. 169 and 164 Ma (Middle Jurassic) for Cal1, and between ca. 149 and 126 Ma (Late Jurassic to Early Cretaceous) for Cal 2. The precipitation timing for Dol1 could be inferred within a time span between ca. 93 and 68 Ma (Late Cretaceous), corresponding to the maximum burial time of the Norian host-rocks. $\delta^{18}O_{fluid}$ were calculated using Tt for each analysed carbonate phase and mean $\delta^{18}O$ values measured for that phase in the same sample (Table 2). Accordingly, the $\delta^{18}O_{fluid}$ are 3.3‰–3.7‰ (mean = 3.5‰) for Cal1, 4.3‰–6.2‰ (mean = 5.3‰) for Cal2, and 1.3‰ for Dol1.

The second scenario is based on the simultaneously measured $T(\Delta_{47})$ and $\delta^{18}O$ (Table 4; Figure 13b) assuming that none of the carbonate phases underwent Δ_{47} reordering, as predicted by the implementation of the models of Hemingway and Henkes (2021) and Passey and Henkes (2012) (Figure 12a,d). Precipitation timing vary from ca. 186 to 150 Ma (Early to Late Jurassic) for Cal1, and from ca. 173 to 149 Ma (Middle to Late Jurassic) for Cal 2. The $T(\Delta_{47})$ measured for Dol1 (119 ± 11°C) overlap the thermal maximum reached by the Norian succession during Late Cretaceous time (ca. 95–67 Ma). $\delta^{18}O_{fluid}$ were calculated using $T(\Delta_{47})$ and $\delta^{18}O$ values simultaneously measured for each carbonate phase. Calculated $\delta^{18}O_{fluid}$ values are 1.2‰– 4.2‰ (mean = 2.7‰) for Cal1, 1.8‰–2.2‰ (mean = 2.0‰) for Cal2 and 2.2‰ for Dol1.

The third scenario was reconstructed with different approaches based on the mineralogy of the investigated phases and on the implementation of Stolper and Eiler (2015) reordering model (Figure 12c). For Cal1 and Cal2 we used original precipitation temperatures back calculated from apparent $T(\Delta_{47})$, assuming the calcites underwent Δ_{47} reordering (Figure 12b,c). Accordingly, calcite precipitation could have occurred from ca. 180 to 160 Ma (Early to Late Jurassic) for Cal1, and from ca. 170 to 160 Ma (Middle to Late Jurassic) for Cal2. Diversely, for Dol1 we used the measured $T(\Delta_{47})$ considering that dolomites escaped Δ_{47} reordering. Like for the second scenario, here the

A

	Phase	Sample	Temperature (°C)	Age (Ma)	$\delta^{18}O_{fluid}$ (‰,SMOW)
Tt	Cal 1	LOL 2008	64	~169	3.7
	Cal 1	LOL 8-9	64	~169	3.6
	Cal 1	AR1 18-19	64	~164	3.3
Tt	Cal 2	LOL 2008	76	~149	4.3
	Cal 2	LOL 8-9	93	~126	6.2
Tt	Dol 1	FEX 2396	110	93/68	1.3

B

	Phase	Sample	Temperature (°C)	Age (Ma)	$\delta^{18}O_{fluid}$ (‰,SMOW)
$T\Delta_{47}$	Cal 1	LOL 2008	59±8	180-165	3.4
	Cal 1	AR1 18-19	51±8	186-169	1.2
	Cal 1	AR1 17-18	72±8	164-150	4.2
$T\Delta_{47}$	Cal 2	LOL 2008	77±9	164-149	2.2
	Cal 2	LOL 8-9	63±7	173-163	1.8
$T\Delta_{47}$	Dol 1	FEX 2396	119±11	95-67	2.2

C

	Phase	Temperature (°C)	Age (Ma)	$\delta^{18}O_{fluid}$ (‰,SMOW)
$T\Delta_{47}$	Cal 1	50-70	180-160	0.6 - 4.7
$T\Delta_{47}$	Cal 2	60-70	170-160	-0.6 - 2.3
$T\Delta_{47}$	Dol 1	119±11	95-67	2.2

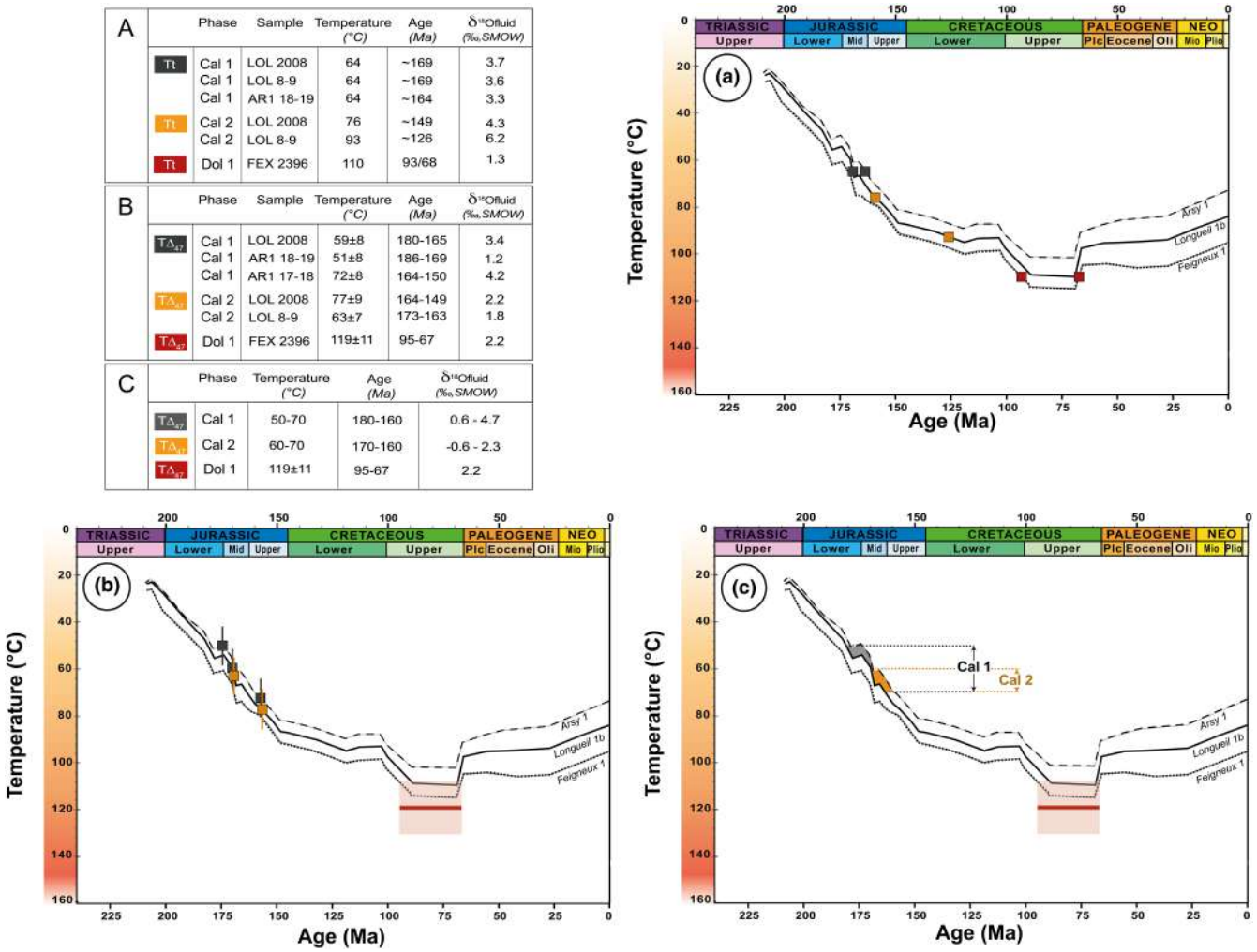

FIGURE 13 Precipitation timing and $\delta^{18}O_{fluid}$ for Cal1, Cal2 and Dol1 obtained according to different temperature datasets produced from FIM and Δ_{47} thermometry and the thermal curves for the Upper Triassic (Norian) succession of the three studied wells extracted from the available 3D basin thermal model under TemisFlow™ (Torelli et al., 2020). (a) Trapping temperatures (Tt) derived from minimum Th values from FIM after pressure correction. (b) Precipitation temperatures from measured $T(\Delta_{47})$ when considering the Passey and Henkes (2012) and the Hemingway and Henkes (2021) reordering models. Vertical bars indicate $T(\Delta_{47})$ uncertainties reported at the 95% confidence level. (c) Cal1 and Cal2 precipitation temperatures back-calculated from apparent $T(\Delta_{47})$ when considering the Stolper and Eiler (2015) reordering model. Dol1 precipitation temperature corresponds to the measured $T(\Delta_{47})$.

Dol1 precipitation temperatures (119 ± 11°C) overlap the Norian succession thermal maximum so that Dol1 precipitation may have occurred during Late Cretaceous time (ca. 95–67 Ma). Calculated $\delta^{18}O_{fluid}$ values are 0.6‰–4.7‰ for Cal1, −0.6‰–2.3‰ for Cal2 and 2.2‰ for Dol1.

From the three above scenarios different precipitation sequences and fluid evolutions may be deduced. The first scenario, based on Tt of FI, suggests that Cal1, Cal2 and Dol1 precipitated sequentially during burial, with Cal2 precipitation spanning over a time interval of 23 My (Figure 13a), and that the parent fluids recorded a depletion in ^{18}O going from Cal1/Cal2 towards Dol1.

The second and third scenarios, based on $T\Delta_{47}$ and by considering different Δ_{47} reordering models (Hemingway & Henkes, 2021; Passey & Henkes, 2012; Stolper & Eiler, 2015), reveal a partial overlap between Cal1 and Cal2 precipitation ages (Figure 13b,c) that are followed by Dol1 from fluids having $\delta^{18}O_{fluid}$ comparable to those of the calcites.

We do not favour the first scenario due to: (1) the uncertainties associated with Tt calculation from minimum Th (Section 5.2; Figure 11); (2) the extremely long precipitation interval inferred for Cal2 which is not accompanied by any change in CL response (Figure 5); (3) the depletion in ^{18}O recorded by Dol1 fluids suggesting dilution which contrasts with the slightly higher salinities recorded in FI from Dol1 (Figure 10). With the present knowledge on calcite Δ_{47} reordering it is not possible to favour a scenario between the second and the third and both scenarios can be considered realistic.

The datasets here presented wants to point at the different precipitation timing and fluid evolutions that would be inferred by relying on each of the discussed scenarios separately (Figure 13). These results underline how processes potentially undermining the reliability of FIM and Δ_{47} data, such as thermal reequilibration and solid-state reordering, need to be carefully evaluated for an accurate reconstruction of thermal and fluid-flow histories in sedimentary basins.

Consistencies versus discrepancies among Th/Tt and T(Δ_{47}), jointly analysed on the same diagenetic carbonates, have been already reported by previous authors (Honlet et al., 2018; Jautzy et al., 2021; MacDonald et al., 2018; Mangenot et al., 2017). In particular, previous studies from the Paris Basin sub-surface used the same sampling and analytical procedures of the present survey to investigate burial diagenetic carbonate phases (Mangenot et al., 2017; Mangenot, Gasparrini, Rouchon, & Bonifacie, 2018). These authors investigated a Middle Jurassic reservoir unit from the basin depocenter that underwent a thermal maximum of ca. 90°C during the Late Cretaceous (Mangenot, Gasparrini, Gerdes, et al., 2018; Mangenot, Gasparrini, Rouchon, & Bonifacie, 2018). The results illustrate a striking mutual consistency between FI and Δ_{47} thermometry data from both calcite and dolomite phases. It derives that under the thermal conditions experienced by these Middle Jurassic rocks, FI did not experience thermal reequilibration and Δ_{47} compositions escaped solid-state reordering. This is also supported by the application of the three different reordering models previously introduced; indeed, none of them predicts carbonate Δ_{47} reordering when considering the thermal histories reported for these Middle Jurassic rocks (Mangenot, Gasparrini, Rouchon, & Bonifacie, 2018). This was the starting point of the present study that wanted to investigate a rock succession from the same basin which experienced a more severe thermal history. The choice of the investigated samples was therefore governed by the search of a cored stratigraphic interval which had experienced more severe thermal conditions compared the one investigated by Mangenot et al. (2017, 2018), (see details in Sections 1 and 3.1). The samples investigated in this study come from a lower stratigraphic interval (at higher depths) and experienced a thermal maximum >100°C (see details in Section 5.3 and Figure 13). Here the main conclusions are that many FI underwent thermal reequilibration, whereas the Δ_{47} solid-state reordering may or may not have occurred depending on the reordering model considered and on the sample mineralogy (see Section 5.3). It derives that when dealing with a succession having experienced thermal maximum >100°C, accuracy and interpretation of FIM and Δ_{47} data (especially on calcite) may be biased by thermal reequilibration and solid-state reordering. In these cases, it is recommended to jointly apply these methods on the same carbonate phases to evaluate mutual consistency of the thermometric data and to combine Δ_{47} analyses with thermal history reordering models, aiming to consider the different possible precipitation scenarios.

5.5 | Insights on fluid origins and carbonate precipitation events

Previous studies of the Chaunoy Fm. focused on the Paris Basin depocenter and have documented burial diagenetic carbonates and attempted to reconstruct the corresponding fluid-flow history (Demars, 1994; Demars & Pagel, 1994; Spötl et al., 1993; Worden et al., 1999). Conversely, to date, no study has investigated the diagenetic evolution of the Chaunoy Fm. reservoirs located to the North of the depocenter. A by-product of the present survey is, therefore, the characterization of the diagenetic history of the Chaunoy Fm. in an underexplored portion of the northern Paris Basin (Figure 1) and specifically the assessment of possible precipitation temperatures and timing of diagenetic carbonates together with the composition of the fluids (salinity, $\delta^{18}O_{fluid}$) from which the carbonates precipitated (Figures 9, 10 and 13). Aiming to bring some insights on paleo-fluid origins and carbonate precipitation, the data issued from this study (and specifically the scenarios issued from the Δ_{47} data that we favour; see Section 5.4 and Figure 13b–d) were here integrated within the fluid-flow reconstructions proposed by the previous authors.

The foregoing works mostly agree on the origin of the parent fluids which precipitated different diagenetic carbonates during burial. Accordingly, the carbonate parent fluids derived from the original formation waters reflecting the continental origin of the Chaunoy Fm. that formed in semi-arid to arid conditions (Bourquin et al., 1998; Spötl & Wright, 1992; Worden et al., 1999). These continental fluids were saline, probably concentrated by evaporation, and most likely associated with pedogenesis (Spötl & Wright, 1992). During burial, they acquired higher $\delta^{18}O_{fluid}$ and salinity due to mixing with halite-saturated brines that migrated from the eastern part of the basin (where thick halite deposits, time equivalent to the Chaunoy Fm., occur (Figure 2; Geisler-Cussey, 1986)) into the Upper Triassic reservoirs to the West. This migration was firstly explained by a brine influx model (Fontes & Matray, 1993; Matray et al., 1989) though its timing is debated in literature. Based on formation water geochemistry, mineral diagenesis and authigenic illite dating, an Early Jurassic time has been

proposed for a first brine migration, followed by a major migration during the Late Jurassic (Matray et al., 1989). Successively, an Early Cretaceous brine migration was proposed based on illite dating (Spötl et al., 1993). Finally, a Late Cretaceous time was proposed based on FI microthermometry combined with thermal modelling (Worden et al., 1999).

In this study, burial diagenetic carbonates within the Chaunoy Fm. (Cal1, Cal2 and Dol1) were investigated from wells located to the NW of the basin depocenter (Figure 1b). These burial carbonate phases display $\delta^{13}C$, $\delta^{18}O_{fluid}$ and salinity comparable with those of burial carbonates (predominantly dolomites) reported by the previous diagenesis studies (Demars, 1994; Demars & Pagel, 1994; Spötl et al., 1993; Worden et al., 1999). The consistently negative $\delta^{13}C$ of these phases (Figure 6; Table 2) is in line with original formation waters of continental origin having interacted with light ^{12}C from soils, formed in semi-arid conditions. The high $\delta^{18}O_{fluid}$ and salinity of Cal1, Cal2 and Dol1 parent fluids (Figure 10; Table 4) reflect the composition of the brines from the East that became enriched in ^{18}O after long interaction with the evaporitic succession. Based on the carbonate precipitation scenarios derived from $T(\Delta_{47})$ data (see Section 5.4 and Figure 13b–d) an Early to Late Jurassic timing for Cal1 and Cal2 precipitation is inferred. This timing is rather in agreement with the scenario initially proposed by Matray et al. (1989) for the brine migration. Diversely, precipitation timing inferred for Dol1 (see Section 5.4 and Figure 13b–d) points to a Late Cretaceous event, which agrees with the timing proposed by Worden et al. (1999).

The different precipitation timing inferred for Cal1 and Cal 2 (Early to Late Jurassic) and for Dol1 (Late Cretaceous) rather suggests a westward brine migration that occurred in pulses and that was possibly triggered by different mechanisms.

During the Early-Middle Jurassic, the basin experienced a relatively rapid subsidence (up to 20–25 m/Ma; Perrodon & Zabek, 1991) mainly as a result of the Mid-Cimmerian phase which records both the early stage of the rise of the thermal dome in the central North Sea (Middle Cimmerian Unconformity) and a further step on the Tethys ocean accretion (Guillocheau et al., 2000; Perrodon & Zabek, 1991). In this setting, the sagging geometry of the basin (Figure 1c) could have permitted the westward migration of brines from the Triassic evaporitic deposits towards the stratigraphically adjacent Chaunoy Fm. (see Figure 2) and explain the precipitation of Cal1 and Cal2. On the other hand, during the Early Cretaceous, a major hiatus occurred in the basin because of Late Cimmerian tectonism, which terminated the carbonate-dominated Late Jurassic depositional regime (Matray et al., 1989; Ziegler, 1990). During this time the NE Vosgues-Rhine block was uplifted allowing the establishment of a gravity-driven fluid-flow that displaced the interstitial brine of the Triassic evaporites towards the west (Perrodon & Zabek, 1991). This event could have been responsible for Dol1 precipitation during the Late Cretaceous.

At last, it is worth stressing the fact that in the previous studies addressing the Chaunoy Fm. diagenesis, burial calcites were not recorded (Demars, 1994; Demars & Pagel, 1994), or are poorly voluminous (Spötl et al., 1993; Worden et al., 1999). Conversely, Cal1 and Cal2 represent the most abundant diagenetic phases in the studied sector, likely affecting the reservoir properties. These findings may assist the ongoing evaluation of the Chaunoy Fm. geothermal potential in the northern Paris Basin.

6 | CONCLUSIONS

Multiple diagenetic carbonates were recognized in subsurface cores from the Upper Triassic (Norian) siliciclastic Chaunoy Fm. of the northern Paris Basin: a reservoir unit that experienced a thermal maximum >100°C in the studied sector. Based on petrography, O-C isotope geochemistry together with fluid inclusion and clumped isotope (Δ_{47}) thermometry, two main calcites and one dolomite, precipitated during burial diagenesis, were distinguished. The carbonate precipitation timing was established by combining the known thermal history of the host succession with the thermal data from fluid inclusion and Δ_{47} compositions and by considering the three existing Δ_{47} reordering models. This approach led to different scenarios in terms of carbonate precipitation timing and parent fluid composition. The results primarily underline the complexity of confidently reconstructing thermal and fluid-flow histories in sedimentary basins. More specifically they underline that in samples having experienced thermal maximum >100°C, accuracy and interpretation of fluid inclusion and Δ_{47} thermometry data (especially on calcite) may be biased by thermal reequilibration and solid-state reordering. The joint application of these methods on the same carbonate phases is highly recommended to assess mutual consistency of the thermometric data and must include an accurate evaluation of processes (such as inclusion thermal reequilibration and Δ_{47} solid-state reordering) that may undermine the accuracy of the results.

The most likely carbonate precipitation scenario includes: (1) two blocky calcites formed during Early to Late Jurassic time; (2) one saddle dolomite formed during the Late Cretaceous. The diagenetic carbonates precipitated from original continental formation waters mixing with brines migrated from the eastern part of the basin where thick evaporitic deposits occur. The timing

inferred for the precipitation of the burial diagenetic carbonate phases finds support from some of the previous studies on the diagenesis of the Upper Triassic units of the Paris Basin.

ACKNOWLEDGEMENTS

Petrography and fluid inclusion studies were completed at the petrography and diagenesis laboratory of IFP Energies nouvelles (France). Thin Section Lab (TSL) is acknowledged for high-quality thin and thick section preparation. Prof. M. Joachimski (GeoZentrum Nordbayern) is thanked for O-C stable isotope analysis of carbonates. Nathan Looser and Madalina Jaggi from ETH-Zurich are thanked for their assistance during Δ_{47} sample preparation and analysis. The cores of Longueil1b, Arsy1 and Feigneux1 wells were available from the IFP Energies nouvelles storage collection of the BEPH (*Bureau Exploration-Production d'Hydrocarbures*). We are grateful to Jean-Pierre Girard (Total) and Tiphaine Marsaux and François-André Duboin (International Petroleum Corp.) for sharing their knowledge on the petroleum reservoirs of the Paris Basin, and to Vanessa Telès (IFP Energies nouvelles) for fruitful discussion on 3D numerical thermal modelling. Warm thanks go to Xavier Mangenot who kindly introduced the first author to the pending issues of his precursor PhD project. This research was undertaken during the first author's PhD project, funded by: MIUR grants to Roma Tre PhD School in Earth Sciences (XXXIV doctoral cycle, 2018–2021) and IFP Energies nouvelles PhD program. The PhD project benefitted from the joint supervision established between Università Roma Tre (Rome) and Sorbonne Université (Paris). We thank the editor Atle Rotevatn for kindly handling this manuscript. Francois Roure, Carlo Bertok and four other anonymous reviewers are thanked for their constructive comments on early versions of the manuscript.

CONFLICT OF INTEREST STATEMENT

There are no conflicts of interest to declare.

DATA AVAILABILITY STATEMENT

The data that support the findings of this study are included in the Supplementary Materials. Further data can be requested to the authors.

ORCID

Natalia A. Vergara Sassarini https://orcid.org/0000-0003-2693-3346
Marta Gasparrini https://orcid.org/0000-0003-3438-4922
Stefano M. Bernasconi https://orcid.org/0000-0001-7672-8856
Sveva Corrado https://orcid.org/0000-0001-9727-9973

REFERENCES

Allan, J. R., & Wiggings, W. D. (1993). Dolomite reservoirs: Geochemical techniques for evaluating origin and distribution. *AAPG Continuing Education Course Notes Series*, *36*, 129.

Anderson, N. T., Kelson, J. R., Kele, S., Daëron, M., Bonifacie, M., Horita, J., Mackey, T. J., John, C. M., Kluge, T., Petschnig, P., Jost, A. B., Huntington, K. W., Bernasconi, S. M., & Bergmann, K. D. (2021). A unified clumped isotope thermometer calibration (0.5-1,100°C) using carbonate based standardization. *Geophysical Research Letters*, *48*(7), e92069. https://doi.org/10.1029/2020GL092069

André, G., Hibsch, C., Fourcade, S., Cathelineau, M., & Buschaert, S. (2010). Chronology of fracture sealing under a meteoric fluid environment: Microtectonic and isotopic evidence of major Cainozoic events in the eastern Paris Basin (France). *Tectonophysics*, *490*(3–4), 214–228. https://doi.org/10.1016/j.tecto.2010.05.016

Bakker, R. J. (2003). Package FLUIDS 1. Computer programs for analysis of fluid inclusion data and for modelling bulk fluid properties. *Chemical Geology*, *194*(1–3), 3–23. https://doi.org/10.1016/S0009-2541(02)00268-1

Bakker, R. J. (2009). Package FLUIDS. Part 3: Correlations between equations of state, thermodynamics and fluid inclusions. *Geofluids*, *9*(1), 63–74. https://doi.org/10.1111/j.1468-8123.2009.00240.x

Beaudoin, N., Gasparrini, M., David, M. E., Lacombe, O., & Kohen, D. (2019). Bedding-parallel stylolites as a tool to unravel maximum burial depth in sedimentary basins: Application to Middle Jurassic carbonate reservoirs in the Paris Basin. *GSA Bulletin*, *131*(7–8), 1239–1254. https://doi.org/10.1130/B32064.1

Bernasconi, S. M., Daëron, M., Bergmann, K. D., Bonifacie, M., Meckler, A. N., Affek, H. P., Anderson, N., Bajnai, D., Barkan, E., Beverly, E., Blamart, D., Burgener, L., Calmels, D., Chaduteau, C., Clog, M., Davidheiser-Kroll, B., Davies, A., Dux, F., Eiler, J., … Ziegler, M. (2021). InterCarb: A community effort to improve interlaboratory standardization of the carbonate clumped isotope thermometer using carbonate standards. *Geochemistry, Geophysics, Geosystems*, *22*, e2020GC009588. https://doi.org/10.1029/2020GC009588

Bernasconi, S. M., Müller, I. A., Bergmann, K. D., Breitenbach, S. F., Fernandez, A., Hodell, D. A., & Ziegler, M. (2018). Reducing uncertainties in carbonate clumped isotope analysis through consistent carbonate-based standardization. *Geochemistry, Geophysics, Geosystems*, *19*(9), 2895–2914. https://doi.org/10.1029/2017GC007385

Blaise, T., Barbarand, J., Kars, M., Ploquin, F., Aubourg, C., Brigaud, B., Cathelineau, C., El Albani, A., Gautheron, C., Izart, A., Janots, D., Michels, R., Pagel, M., Pozzi, J., Boiron, M., & Landrein, P. (2014). Reconstruction of low temperature (<100°C) burial in sedimentary basins: A comparison of geothermometer in the intracontinental Paris Basin. *Marine and Petroleum Geology*, *53*, 71–87. https://doi.org/10.1016/j.marpetgeo.2013.08.019

Bodnar, R. J. (1993). Revised equation and table for determining the freezing point depression of H_2O-NaCl solutions. *Geochimica et Cosmochimica Acta*, *57*(3), 683–684. https://doi.org/10.1016/0016-7037(93)90378-A

Bodnar, R. J. (2003). Reequilibration of fluid inclusions. In I. Samson, A. Anderson, & D. Marshall (Eds.), *Fluid inclusions: Analysis*

and interpretation (Vol. *32*, pp. 213–231). Mineralogical Association of Canada Short Course.

Bodnar, R. J., & Vityk, M. O. (1994). Interpretation of microthermometric data for H_2O-NaCl fluid inclusions. In B. De Vivo & M. L. Frezzotti (Eds.), *Fluid inclusions in minerals: Methods and applications* (pp. 117–130). Pontignsno-Siena.

Boissavy, C., & Grière, O. (2014). New geothermal targets in the Paris Basin (France). *GRC Transactions*, *38*, 577–582.

Bonté, D., van Wees, J.-D., Guillou-Frottier, L., Bouchot, V., & Serrano, O. (2013). Deep temperatures in the Paris Basin using tectonic-heat flow modelling. European Geothermal Congress EGC 2013, June 2013, Pise, Italy. 10 p. ffhal-00842726.

Bourquin, S., Boehm, C., Clermonte, J., Durand, M., & Serra, O. (1993). Facies and sequence-analysis of the Triassic series in the west-Central Paris Basin, using wireline logs. *Bulletin De La Societe Geologique De France*, *164*(2), 177–188. https://doi.org/10.1016/0037-0738(95)00153-0

Bourquin, S., Rigollet, C., & Bourges, P. (1998). High-resolution sequence stratigraphy of an alluvial fan–fan delta environment: Stratigraphic and geodynamic implications–An example from the Keuper Chaunoy Sandstones, Paris Basin. *Sedimentary Geology*, *121*(3–4), 207–237. https://doi.org/10.1016/S0037-0738(98)00081-5

Bourquin, S., Vairon, J., & Le Strat, P. (1997). Three-dimensional evolution of the Keuper of the Paris basin based on detailed isopach maps of the stratigraphic cycles: Tectonic influences. *Geologische Rundschau*, *86*(3), 670–685. https://doi.org/10.1007/s005310050170

Brenner, D. C., Passey, B. H., & Stolper, D. A. (2018). Influence of water on clumped-isotope bond reordering kinetics in calcite. *Geochimica et Cosmochimica Acta*, *224*, 42–63. https://doi.org/10.1016/j.gca.2017.12.026

Brigaud, B., Bonifacie, M., Pagel, M., Blaise, T., Calmels, D., Haurine, F., & Landrein, P. (2020). Past hot fluid flows in limestones detected by Δ_{47}–(U-Pb) and not recorded by other geothermometers. *Geology*, *48*(9), 851–856. https://doi.org/10.1130/G47358.1

Brunet, M. F., & Le Pichon, X. (1982). Subsidence of the Paris basin. *Journal of Geophysical Research: Solid Earth*, *87*(B10), 8547–8560. https://doi.org/10.1029/JB087iB10p08547

Cavelier, C., & Lorenz, J. (1987). *Aspect et évolution geologiques du Bassin Parisien*. Bull Inf. Bassin. Paris. hors serie no. 6.

Clauer, N., O'Neil, J. R., & Furlan, S. (1995). Clay minerals as records of temperature conditions and duration of thermal anomalies in the Paris Basin, France. *Clay Minerals*, *30*, 1–13.

Corrado, S., Vergara Sassarini, N. A., Schito, A., Michel, P., & Gasparrini, M. (2022). New integrated geochemical and petrographic constraints to paleo-thermal and paleo-environmental reconstructions from organic matter dispersed in the early Toarcian organic-rich shales of the Paris Basin (France) [abstract]. SGI-SIMP Congress; 2022 September 19–21; Torino, Italy. Abstract n. 825 https://doi.org/10.3301/ABSGI.2022.02

Daëron, M., Blamart, D., Peral, M., & Affek, H. P. (2016). Absolute isotopic abundance ratios and the accuracy of Δ_{47} measurements. *Chemical Geology*, *442*, 83–96. https://doi.org/10.1016/j.chemgeo.2016.08.014

Dassié, E. P., Genty, D., Noret, A., Mangenot, X., Massault, M., Lebas, N., Duhamel, M., Bonifacie, M., Gasparrini, M., Minster, B., & Michelot, J. L. (2018). A newly designed analytical line to examine fluid inclusion isotopic compositions in a variety of carbonate samples. *Geochemistry, Geophysics, Geosystems*, *19*(4), 1107–1122. https://doi.org/10.1002/2017GC007289

Delmas, J., Houel, P., & Vially, R. (2002). *Paris Basin. Rapport régional d'évaluation pétrolière*. IFPEN intern report (pp. 172).

Demars, C. (1994). *Évolution diagénétique, paléofluides et paléothermicité dans les réservoirs du Keuper et du Dogger du bassin de Paris* (pp. 325). Thesis, INPL.

Demars, C., & Pagel, M. (1994). Paléotempératures et paléosalinités dans les grès du Keuper du Bassin de Paris: Inclusions fluides dans les minéraux authigènes. *Comptes Rendus de l'Académie des Sciences. Série 2. Sciences de la Terre et des Planètes*, *319*(4), 427–434.

Dennis, K. J., & Schrag, D. P. (2010). Clumped isotope thermometry of carbonatites as an indicator of diagenetic alteration. *Geochimica et Cosmochimica Acta*, *74*(14), 4110–4122. https://doi.org/10.1016/j.gca.2010.04.005

Deschamps, R., Kohler, E., Gasparrini, M., Durand, O., Euzen, T., & Nader, F. H. (2012). Impact of mineralogy and diagenesis on reservoir quality of the Lower Cretaceous Upper Mannville Formation (Alberta, Canada). *Oil & Gas Science and Technology*, *67*(1), 31–58. https://doi.org/10.2516/ogst/2011153

Dickson, J. A. D. (1966). Carbonate identification and genesis as revealed by staining. *Journal of Sedimentary Research*, *36*(2), 491–505. https://doi.org/10.1306/74D714F6-2B21-11D7-8648000102C1865D

Eiler, J. M. (2007). "Clumped-isotope" geochemistry—The study of naturally-occurring, multiply-substituted isotopologues. *Earth and Planetary Science Letters*, *262*(3–4), 309–327. https://doi.org/10.1016/j.epsl.2007.08.020

Espitalié, J., Maxwell, J. R., Chenet, Y., & Marquis, F. (1988). Aspects of hydrocarbon migration in the Mesozoic in the Paris Basin as deduced from an organic geochemical survey. *Organic Geochemistry*, *15*, 467–481. https://doi.org/10.1016/B978-0-08-037236-5.50054-3

Fernandez, A., Müller, I. A., Rodríguez-Sanz, L., van Dijk, J., Looser, N., & Bernasconi, S. M. (2017). A reassessment of the precision of carbonate clumped isotope measurements: Implications for calibrations and paleoclimate reconstructions. *Geochemistry, Geophysics, Geosystems*, *18*(12), 4375–4386. https://doi.org/10.1002/2017GC007106

Ferry, J. M., Passey, B. H., Vasconcelos, C., & Eiler, J. M. (2011). Formation of dolomite at 40–80°C in the Latemar carbonate buildup, Dolomites, Italy, from clumped isotope thermometry. *Geology*, *39*, 571–574. https://doi.org/10.1130/G31845.1

Flügel, E. (2004). *Microfacies of carbonate rocks: Analysis, interpretation and application* (p. 976). Springer Science and Business Media. https://doi.org/10.1007/978-3-662-08726-8

Fontes, J. C., & Matray, J. M. (1993). Geochemistry and origin of formation brines from the Paris Basin, France: 1. Brines associated with Triassic salts. *Chemical Geology*, *109*(1–4), 149–175.

Gabellone, T., Gasparrini, M., Iannace, A., Invernizzi, C., Mazzoli, S., & D'Antonio, M. (2013). Fluid channelling along thrust zones: The Lagonegro case history, southern Apennines, Italy. *Geofluids*, *13*(2), 140–158. https://doi.org/10.1111/gfl.12020

Gable, R. (1978). *Acquisition et rassemblement de données géothermiques disponibles en France*. Contrat 170-76 egf - projet g/a 5 Bureau de Recherches Géologiques et Minières. Report BRGM/78-SGN-284-GTH, 60 p. 1 pht., 10 maps.

Gasparrini, M., Lacombe, O., Rohais, S., Belkacemi, M., & Euzen, T. (2021). Natural mineralized fractures from the Montney-Doig

unconventional reservoirs (Western Canada Sedimentary Basin): Timing and controlling factors. *Marine and Petroleum Geology*, *124*, 104826. https://doi.org/10.1016/j.marpetgeo.2020.104826

Gasparrini, M., Morad, D., Mangenot, X., Bonifacie, M., Morad, S., Nader, F. H., & Gerdes, A. (2023). Dolomite recrystallization revealed by Δ_{47}/U-Pb thermochronometry in the Upper Jurassic Arab Formation, United Arab Emirates. *Geology*, *51*(5), 471–475. https://doi.org/10.1130/G50960.1

Gasparrini, M., Ruggieri, G., & Brogi, A. (2013). Diagenesis versus hydrothermalism and fluid–rock interaction within the Tuscan Nappe of the Monte Amiata CO_2-rich geothermal area (Italy). *Geofluids*, *13*(2), 159–179. https://doi.org/10.1111/gfl.12025

Gaulier, J. M., & Burrus, J. (1994). Modeling present and past thermal regimes in the Paris Basin: Petroleum implications. In A. Mascle (Ed.), *Hydrocarbon and petroleum geology of France* (pp. 61–73). Springer. https://doi.org/10.1007/978-3-642-78849-9_5

Geisler-Cussey, D. (1986). *Approche sédimentologique et géochimique des mécanismes générateurs de formations évaporitiques actuelles et fossiles. Marais salants de Camargue et du Levant Espagnol, Messinien méditerranéen et Trias lorrain* (pp. 268). Thesis, Sci. de la Terre.

Gély, J. P., & Hanot, F. (2014). *Le Bassin parisien: Un nouveau regard sur la géologie* (Vol. *9*, p. 229). https://books.google.it/books/about/Le_bassin_parisien.html?id=tyL-rQEACAAJ&redir_esc=y

Ghosh, P., Adkins, J., Affek, H., Balta, B., Guo, W., Schauble, E. A., Schrag, D., & Eiler, J. M. (2006). ^{13}C–^{18}O bonds in carbonate minerals: A new kind of paleothermometer. *Geochimica et Cosmochimica Acta*, *70*(6), 1439–1456. https://doi.org/10.1016/j.gca.2005.11.014

Goldstein, R. H. (2001). Fluid inclusions in sedimentary and diagenetic systems. *Lithos*, *55*(1–4), 159–193. https://doi.org/10.1016/S0024-4937(00)00044-X

Goldstein, R. H. (2003). Petrographic analysis of fluid inclusions. In I. Samson, A. Anderson, & D. Marshall (Eds.), *Fluid inclusions: Analysis and interpretation* (Vol. *32*, pp. 9–53). Mineralogical Association of Canada.

Goldstein, R. H., & Reynolds, J. T. (1994). *Systematics of fluid inclusions in diagenetic minerals* (Vol. *31*, pp. 160). SEPM Short Course.

Gonçalvès, J., Pagel, M., Violette, S., Guillocheau, F., & Robin, C. (2010). Fluid inclusions as constraints in a three-dimensional hydro-thermo-mechanical model of the Paris Basin, France. *Basin Research*, *22*(5), 699–716. https://doi.org/10.1111/j.1365-2117.2009.00428.x

Guilhaumou, N. (1993). Paleotemperatures inferred from fluid inclusions in diagenetic cements: Implications for the thermal history of the Paris Basin. *European Journal of Mineralogy*, *5*, 1217–1226. https://doi.org/10.1016/j.marpetgeo.2020.104487

Guilhaumou, N., & Gaulier, J. M. (1991). Détermination de paléotempératures dans les roches-mères du bassin de Paris: Étude d'inclusions fluides et implications pour l'histoire thermique du bassin. *Comptes rendus de l'Académie des Sciences. Série 2, Mécanique, Physique, Chimie, Sciences de l'univers, Sciences de la Terre*, *313*(7), 773–780.

Guillocheau, F., Robin, C., Allemand, P., Bourquin, S., Brault, N., Dromart, G., Friendenberg, R., Garcia, J. P., Gaulier, J. M., Gaumet, F., Grosdoy, B., Hanot, F., Le Strat, P., Mettraux, M., Nalpas, T., Prijac, C., Rigoltet, C., Serrano, O., & Grandjean, G. (2000). Meso-Cenozoic geodynamic evolution of the Paris Basin: 3D stratigraphic constraints. *Geodinamica Acta*, *13*(4), 189–245.

Hanor, J. S. (1984). Variation in chemical composition of oil field brines with depth in northern Louisiana and southern Arkansas: Implications for mechanisms and rates of mass transport and diagenetic reaction. *AAPG Bulletin*, *68*(9), 1212–1213. https://doi.org/10.1306/AD4617F0-16F7-11D7-8645000102C1865D

Hemingway, J. D. (2020). *Isotopylog: Open-source tools for clumped isotope kinetic data analysis.* https://doi.org/10.5281/zenodo.4005822

Hemingway, J. D., & Henkes, G. A. (2021). A disordered kinetic model for clumped isotope bond reordering in carbonates. *Earth and Planetary Science Letters*, *566*, 116962. https://doi.org/10.1016/j.epsl.2021.116962

Henkes, G. A., Passey, B. H., Grossman, E. L., Shenton, B. J., Pérez-Huerta, A., & Yancey, T. E. (2014). Temperature limits for preservation of primary calcite clumped isotope paleotemperatures. *Geochimica et Cosmochimica Acta*, *139*, 362–382. https://doi.org/10.1016/j.gca.2014.04.040

Honlet, R., Gasparrini, M., Muchez, P., Swennen, R., & John, C. M. (2018). A new approach to geobarometry by combining fluid inclusion and clumped isotope thermometry in hydrothermal carbonates. *Terra Nova*, *30*(3), 199–206. https://doi.org/10.1111/ter.12326

Horita, J. (2014). Oxygen and carbon isotope fractionation in the system dolomite–water–CO_2 to elevated temperatures. *Geochimica et Cosmochimica Acta*, *129*, 111–124. https://doi.org/10.1016/j.gca.2013.12.027

Huntington, K. W., & Petersen, S. V. (2023). Frontiers of carbonate clumped isotope thermometry. *Annual Review of Earth and Planetary Sciences*, *51*, 611–641. https://doi.org/10.1146/annurev-earth-031621-085949

Jaudin, F. (2009). *French geothermal resources survey. BRGM contribution to the market study in the LOW-BIN project* (pp. 57583). BRGM Report.

Jautzy, J. J., Savard, M. M., Lavoie, D., Ardakani, O. H., Dhillon, R. S., Defliese, W. F., & Castagner, A. (2021). Clumped isotope geothermometry of an Ordovician carbonate mound, Hudson Bay Basin. *Journal of the Geological Society*, *178*(1), 2020–2102. https://doi.org/10.1144/jgs2020-102

John, C. M., & Bowen, D. (2016). Community software for challenging isotope analysis: First applications of 'Easotope' to clumped isotopes. *Rapid Communications in Mass Spectrometry*, *30*(21), 2285–2300. https://doi.org/10.1002/rcm.7720

Kharaka, Y. K., & Hanor, J. S. (2003). 5.16 Deep fluids in the continents: 1. Sedimentary basins. In H. D. Holland & K. K. Turekian (Eds.), *Treatise on geochemistry* (pp. 1–48). ISBN 9780080437514). Elsevier Science. https://doi.org/10.1016/B0-08-043751-6/05085-4

Krumgalz, B. S., Pogorelsky, R., & Pitzer, K. S. (1996). Volumetric properties of single aqueous electrolytes from zero to saturation concentration at 298.15 K represented by Pitzer's ion-interaction equations. *Journal of Physical and Chemical Reference Data*, *25*(2), 663–689. https://doi.org/10.1063/1.555981

Lawson, M., Shenton, B. J., Stolper, D. A., Eiler, J. M., Rasbury, E. T., Becker, T. P., Pottorf, R., Grey, G. G., Yurewicz, D., & Gournay, J. (2018). Deciphering the diagenetic history of the El Abra formation of eastern Mexico using reordered clumped isotope

temperatures and U-Pb dating. *GSA Bulletin*, *130*(3–4), 617–629. https://doi.org/10.1130/B31656.1

Ledésert, B. A., Hébert, R. L., Trullenque, G., Genter, A., Dalmais, E., & Herisson, J. (2022). Editorial of special issue "enhanced geothermal systems and other deep geothermal applications throughout Europe: The MEET project". *Geosciences*, *2022*(12), 341. https://doi.org/10.3390/geosciences12090341

Lloyd, M. K. (2020). *ClumpyCool*. OSF. https://doi.org/10.17605/OSF.IO/JYHSW

Lloyd, M. K., Eiler, J. M., & Nabelek, P. I. (2017). Clumped isotope thermometry of calcite and dolomite in a contact metamorphic environment. *Geochimica et Cosmochimica Acta*, *197*, 323–344. https://doi.org/10.1016/j.gca.2016.10.037

Lloyd, M. K., Ryb, U., & Eiler, J. M. (2018). Experimental calibration of clumped isotope reordering in dolomite. *Geochimica et Cosmochimica Acta*, *242*, 1–20. https://doi.org/10.1016/j.gca.2018.08.036

MacDonald, J. M., John, C. M., & Girard, J. P. (2018). Testing clumped isotopes as a reservoir characterization tool: A comparison with fluid inclusions in a dolomitized sedimentary carbonate reservoir buried to 2–4 km. *Geological Society, London, Special Publications*, *468*(1), 189–202. https://doi.org/10.1144/SP468.7

Mangenot, X., Bonifacie, M., Gasparrini, M., Götz, A., Ader, M., & Rouchon, V. (2017). Coupling Δ_{47} and fluid inclusion thermometry on carbonate cements to precisely reconstruct the temperature, salinity and $\delta^{18}O$ of paleo-groundwater in sedimentary basins. *Chemical Geology*, *472*, 44–57. https://doi.org/10.1016/j.chemgeo.2017.10.011

Mangenot, X., Deconinck, J.-F., Bonifacie, M., Rouchon, V., Collin, P. Y., Quesne, D., Gasparrini, M., & Sizun, J.-P. (2019). Thermal and exhumation histories of the northern subalpine chains (Bauges and Bornes – France): Evidence from forward thermal modeling coupling clay mineral diagenesis, organic maturity and carbonate clumped isotope (Δ_{47}) data. *Basin Research*, *31*(2), 361–379. https://doi.org/10.1111/bre.12324

Mangenot, X., Gasparrini, M., Gerdes, A., Bonifacie, M., & Rouchon, V. (2018). An emerging thermo-chronometer for carbonate bearing-rocks: Δ_{47}/(U-Pb). *Geology*, *46*(12), 1067–1070. https://doi.org/10.1130/G45196.1

Mangenot, X., Gasparrini, M., Rouchon, V., & Bonifacie, M. (2018). Basin scale thermal and fluid-flow histories revealed by carbonate clumped isotopes (Δ_{47})—Middle Jurassic of the Paris Basin depocenter. *Sedimentology*, *65*, 123–150. https://doi.org/10.1111/sed.12427

Matray, J. M., Meunier, A., Thomas, M., & Fontes, J. C. (1989). Les eaux de formation du Trias et du Dogger du bassin parisien: Histoire et effets diagénétiques sur les réservoirs. *Bulletin Des Centres de Recherches Exploration-Production Elf-Aquitaine*, *13*(2), 483–504.

Ménétrier, C., Élie, M., Martinez, L., Le Solleuz, A., Disnar, J. R., Robin, C., Guillocheau, F., & Rigollet, C. (2005). Estimation of the maximum burial palaeotemperature for Toarcian and Callovo-Oxfordian samples in the central part of the Paris Basin using organic markers. *Comptes Rendus Géoscience*, *337*, 15–1323. https://doi.org/10.1016/j.crte.2005.07.004

Montano, D., Gasparrini, M., Gerdes, A., Della Porta, G., & Albert, R. (2021). In-situ U-Pb dating of Ries Crater lacustrine carbonates (Miocene, South-West Germany): Implications for continental carbonate chronostratigraphy. *Earth and Planetary Science Letters*, *568*, 117001. https://doi.org/10.1016/j.epsl.2021.117011

Montano, D., Gasparrini, M., Rohais, S., Albert, R., & Gerdes, A. (2022). Depositional age models in lacustrine systems from zircon and carbonate U-Pb geochronology. *Sedimentology*, *69*, 2507–2534. https://doi.org/10.1111/sed.13000

Monticone, B., Duval, M., Knispel, R., Wojciak, P., & Dubille, M. H. (2011). *Shale oil potential of the Paris Basin, France*. 10384. AAPG Int. Conf. Exhib. AAPG.

Moore, C. H. (2001). *Carbonate reservoirs, porosity evolution and diagenesis in a sequence stratigraphic framework* (Vol. *55*, p. 444). Development in Sedimentology.

Morad, S. (1998). Carbonate cementation in sandstones: Distribution patterns and geochemical evolution. In S. Morad (Ed.), *Carbonate cementation in sandstones*. Wiley-Blackwell. https://doi.org/10.1002/9781444304893.ch1; https://www.wiley-vch.de/en/areas-interest/natural-sciences/carbonate-cementation-in-sandstones-978-0-632-04777-2

Morse, J. W., & Mckenzie, F. T. (1990). Geochemistry of sedimentary carbonates. *Developments in Sedimentology*, *48*, 760.

Müller, I. A., Fernandez, A., Radke, J., Van Dijk, J., Bowen, D., Schwieters, J., & Bernasconi, S. M. (2017). Carbonate clumped isotope analyses with the long-integration dual-inlet (LIDI) workflow: Scratching at the lower sample weight boundaries. *Rapid Communications in Mass Spectrometry*, *31*(12), 1057–1066. https://doi.org/10.1002/rcm.7878

Müller, I. A., Violay, M. E., Storck, J. C., Fernandez, A., Van Dijk, J., Madonna, C., & Bernasconi, S. M. (2017). Clumped isotope fractionation during phosphoric acid digestion of carbonates at 70 C. *Chemical Geology*, *449*, 1–14. https://doi.org/10.1016/j.chemgeo.2016.11.030

Naylor, H. N., Defliese, W. F., Grossman, E. L., & Maupin, C. R. (2019). Investigation of the thermal history of the Delaware Basin (West Texas, USA) using carbonate clumped isotope thermometry. *Basin Research*, *32*(5), 1140–1155. https://doi.org/10.1111/bre.12419

O'Neil, J. R., Clayton, R. N., & Mayeda, T. K. (1969). Oxygen isotope fractionation in divalent metal carbonates. *The Journal of Chemical Physics*, *51*(12), 5547–5558. https://doi.org/10.1063/1.1671982

Pages, L. (1987). Exploration of the Paris basin. In J. Brooks & K. Glennie (Eds.), *Petroleum geology of north West Europe* (pp. 87–93). Graham and Trotman.

Passey, B. H., & Henkes, G. A. (2012). Carbonate clumped isotope bond reordering and geospeedometry. *Earth and Planetary Science Letters*, *351*, 223–236. https://doi.org/10.1016/j.epsl.2012.07.021

Perrodon, A., & Zabek, J. (1991). Interior cratonic basins. Analog basins: Paris Basin. *AAPG Memoir*, *51*, 663–679.

Pomerol, C. (1989). Stratigraphy of the Palaeogene: Hiatuses and transitions. *Proceedings of the Geologists' Association*, *100*(3), 313–324. https://doi.org/10.1016/S0016-7878(89)80051-3

Poulet, M., & Espitalié, J. (1987). Hydrocarbon migration in the Paris Basin. In B. Doligez (Ed.), *Migration of hydrocarbons in sedimentary basins* (Vol. 45, pp. 131–171). Institute Francais Du Petrole Publications, Editions Technip.

Roberts, N. M., Drost, K., Horstwood, M. S., Condon, D. J., Chew, D., Drake, H., Milodowski, E. A., McLean, M. N., Smye, E. J., Wlaker, R. J., Haslam, R., Hodson, K., Imber, J., Beaudoin, N., & Lee, J. K. (2020). Laser ablation inductively coupled plasma

mass spectrometry (LA-ICP-MS) U–Pb carbonate geochronology: Strategies, progress, and limitations. *Geochronology*, *2*(1), 33–61. https://doi.org/10.5194/gchron-2-33-2020

Roedder, E., & Bodnar, R. J. (1980). Geologic pressure determinations from fluid inclusion studies. *Annual Review of Earth and Planetary Sciences*, *8*(1), 263–301. https://doi.org/10.1146/annurev.ea.08.050180.001403

Ronchi, P., Jadoul, F., Ceriani, A., Di Giulio, A., Scotti, P., Ortenzi, A., & Previde Massara, E. (2011). Multistage dolomitization and distribution of dolomitized bodies in Early Jurassic carbonate platforms (Southern Alps, Italy). *Sedimentology*, *58*(2), 532–565. https://doi.org/10.1111/j.1365-3091.2010.01174

Rosenbaum, J., & Sheppard, S. M. F. (1986). An isotopic study of siderites, dolomites and ankerites at high temperatures. *Geochimica et Cosmochimica Acta*, *50*(6), 1147–1150. https://doi.org/10.1016/0016-7037(86)90396-0

Ryb, U., Lloyd, M. K., Stolper, D. A., & Eiler, J. M. (2017). The clumped-isotope geochemistry of exhumed marbles from Naxos, Greece. *Earth and Planetary Science Letters*, *470*, 1–12. https://doi.org/10.1016/j.epsl.2017.04.026

Schauble, E. A., Ghosh, P., & Eiler, J. M. (2006). Preferential formation of ^{13}C–^{18}O bonds in carbonate minerals, estimated using first-principles lattice dynamics. *Geochimica et Cosmochimica Acta*, *70*(10), 2510–2529. https://doi.org/10.1016/j.gca.2006.02.011

Sengelen, X., Robion, P., Bourquin, S., Regnet, J.-B., Barnes, C., & Ledésert, B. (2021). Geothermal exploration of upper Triassic deposits in the Paris Basin: Comparison of the sedimentary records and petrophysical properties between in-situ and analogue site (Ardeche, France). Proceedings World Geothermal Congress 2020+1, Reykjavik, Iceland, April–October 2021.

Sengelen, X., Robion, P., Ledésert, B., Hébert, R., Regnet, J. B., Bourquin, S., Gasparrini, M., Margueret, S., & Barnes, C. (2019). Petrophysical characterization of Triassic and basement formations for geothermal purposes in the Paris basin: From sub-surface data to reservoir outcrop analogue. European Geothermal Congress, 11–14 June, Den Haag, the Netherlands.

Sharp, Z. D., & Kirschner, D. L. (1994). Quartz-calcite oxygen isotope thermometry: A calibration based on natural isotopic variations. *Geochimica et Cosmochimica Acta*, *58*, 4491–4501.

Shenton, B. J., Grossman, E. L., Passey, B. H., Henkes, G. A., Becker, T. P., Laya, J. C., Perez-Huerta, A., Becker, P. S., & Lawson, M. (2015). Clumped isotope thermometry in deeply buried sedimentary carbonates: The effects of bond reordering and recrystallization. *GSA Bulletin*, *127*(7–8), 1036–1051. https://doi.org/10.1130/B31169.1

Sibley, D. F., & Gregg, J. M. (1987). Classification of dolomite rock textures. *Journal of Sedimentary Research*, *57*(6), 967–975. https://doi.org/10.1306/212F8CBA-2B24-11D7-8648000102C1865D

Spötl, C. (1996). Clay minerals as records of temperature conditions and duration of thermal anomalies in the Paris Basin, France. *Clay Minerals*, *31*, 203–208.

Spötl, C., Matter, A., & Brevart, O. (1993). Diagenesis and pore water evolution in the Keuper reservoir, Paris Basin (France). *Journal of Sedimentary Research*, *63*(5), 909–928. https://doi.org/10.1306/D4267C44-2B26-11D7-8648000102C1865D

Spötl, C., & Pitman, J. K. (1998). Saddle (baroque) dolomite in carbonates and sandstones: A reappraisal of a burial-diagenetic concept. In *Carbonate cementation in sandstones: Distribution patterns and geochemical evolution* (Vol. *26*, pp. 437–460). Wiley. https://www.wiley.com/en-us/Carbonate+Cementation+in+Sandstones:+Distribution+Patterns+and+Geochemical+Evolution-p-9780632047772

Spötl, C., & Wright, V. P. (1992). Groundwater dolocretes from the Upper Triassic of the Paris Basin, France: A case study of an arid, continental diagenetic facies. *Sedimentology*, *39*(6), 1119–1136. https://doi.org/10.1111/j.1365-3091.1992.tb02000.x

Stolper, D. A., & Eiler, J. M. (2015). The kinetics of solid-state isotope-exchange reactions for clumped isotopes: A study of inorganic calcites and apatites from natural and experimental samples. *American Journal of Science*, *315*(5), 363–411. https://doi.org/10.2475/05.2015.01

Swart, P. K. (2015). The geochemistry of carbonate diagenesis: The past, present and future. *Sedimentology*, *62*(5), 1233–1304. https://doi.org/10.1111/sed.12205

Telès, V., Fornel, A., Houel, P., Delmas, J., Mengus, J. M., Michel, A., & Maurand, N. (2014). Coupling basin and reservoir simulators for an improved CO_2 injection flow model. *Energy Procedia*, *63*, 3665–3675. https://doi.org/10.1016/j.marpetgeo.2020.104487

Torelli, M., Traby, R., Telès, V., & Ducros, M. (2020). Thermal evolution of the intracratonic Paris Basin: Insights from 3D basin modelling. *Marine and Petroleum Geology*, *119*, 104487. https://doi.org/10.1016/j.marpetgeo.2020.104487

Tournier, F., Pagel, M., Portier, E., Wazir, I., & Fiet, N. (2010). Relationship between deep diagenetic quartz cementation and sedimentary facies in a late Ordovician glacial environment (Sbaa Basin, Algeria). *Journal of Sedimentary Research*, *80*(12), 1068–1084. https://doi.org/10.2110/jsr.2010.094

Uriarte, J. A. (1997). *Maturité thermique des sédiments de la bordure sud-est du Bassin de Paris, University of Geneva* (pp. 146, PhD Thesis).

Van Geldern, R., Hayashi, T., Böttcher, M. E., Mottl, M. J., Barth, J. A., & Stadler, S. (2013). Stable isotope geochemistry of pore waters and marine sediments from the New Jersey shelf: Methane formation and fluid origin. *Geosphere*, *9*(1), 96–112. https://doi.org/10.1130/GES00859.1

Vergara Sassarini, N. A. (2022). *New approaches for sedimentary basins thermal calibration: Towards integration of source rocks Raman spectroscopy and carbonate thermometry* (pp. 262, PhD Thesis). Università Roma Tre – Sorbonne Université.

Vergara Sassarini, N. A., Schito, A., Gasparrini, M., Michel, P., & Corrado, S. (2023). Automatic organofacies identification by means of machine learning on Raman spectra. *International Journal of Coal Geology*, *271*, 104237.

Worden, R. H., Armitage, P. J., Butcher, A. R., Churchill, J. M., Csoma, A. E., Hollis, C., Lander, R. H., & Omma, J. E. (2018). Petroleum reservoir quality prediction: Overview and contrasting approaches from sandstone and carbonate communities. *Geological Society, London, Special Publications*, *435*(1), 1–31. https://doi.org/10.1144/SP435.2

Worden, R. H., Coleman, M. L., & Matray, J. M. (1999). Basin scale evolution of formation waters: A diagenetic and formation water study of the Triassic Chaunoy Formation, Paris Basin. *Geochimica et Cosmochimica Acta*, *63*(17), 2513–2528. https://doi.org/10.1016/S0016-7037(99)00121-0

Worden, R. H., & Matray, J. M. (1995). Cross formational flow in the Paris Basin. *Basin Research*, *7*(1), 53–66. https://doi.org/10.1111/j.1365-2117.1995.tb00095.x

Worden, R. H., & Matray, J. M. (1998). Carbonate cement in the Triassic Chaunoy Formation of the Paris Basin: Distribution and

effect on flow properties. *Carbonate Cementation in Sandstones: Distribution Patterns and Geochemical Evolution*, 163–177. Wiley. https://www.wiley.com/en-us/Carbonate+Cementation+in+Sandstones:+Distribution+Patterns+and+Geochemical+Evolution-p-9780632047772; https://doi.org/10.1002/9781444304893.ch7

Ziegler, P. A. (1990). Geological atlas of Western and Central Europe (pp. 130). Shell Inter-nationale Petroleum Maatschappij.

SUPPORTING INFORMATION

Additional supporting information can be found online in the Supporting Information section at the end of this article.

How to cite this article: Vergara Sassarini, N. A., Gasparrini, M., Bernasconi, S. M., & Corrado, S. (2023). Joint application of fluid inclusion and clumped isotope (Δ_{47}) thermometry unravels the complexity of thermal and fluid-flow history reconstruction in sedimentary basins—Upper Triassic Chaunoy Formation reservoirs (Paris Basin). *Basin Research*, *00*, 1–31. https://doi.org/10.1111/bre.12814